Journal Name

ARTICLE TYPE

Cite this: DOI: 00.0000/xxxxxxxxxx

High-temperature elastic moduli: a tool for understanding chemical bonding and thermal transport in thermoelectric materials

Wanyue Peng, Ashiwini Balodhi, Alexandra Zevalkink

Received Date
Accepted Date

DOI: 00.0000/xxxxxxxxxx

The elastic moduli of solids play a central role in determining functional properties mediated by phonons. In the study of thermoelectric materials, elastic moduli can be used to understand as well as predict lattice thermal conductivity and some aspects of the electronic conductivity (e.g., electron-phonon interactions). Elastic moduli are also highly sensitive to the details of chemical bonding and structural arrangement in a material and can be used to detect subtle changes in crystal symmetry or site disorder due to phase transitions. Consequently, measurements of elastic moduli are of fundamental importance in the study of thermoelectric materials and provide an important link in developing structure-property relationships. Experimental characterization of elastic constants in functional materials are still relatively sparse, and temperature-dependent data is even less common. This review compares the temperature-dependent elastic properties of various classes of thermoelectric materials and emphasizes the role that such data can play in interpreting the transport properties and chemical bonding. In particular, we highlight the relationship between the Grüneisen parameter and the rate of softening of materials, and we discuss the use of temperature-dependent measurements to investigate structural phase transitions.

Contents

Keywords: modulus of elasticity, elastic constants, Grüneisen parameter, lattice thermal conductivity, bond stiffness

1 Introduction

Thermoelectric materials - used in the solid-state conversion of heat to electricity and vice-versa[1] - encompass a wide spectrum

---

[a] *Chemical Engineering and Materials Science Department, Michigan State University, East Lancing, MI, USA*

† Electronic Supplementary Information (ESI) available: [details of any supplementary information available should be included here]. See DOI: 10.1039/b000000x/

of material chemistries, ranging from semiconductors to semimetals, ceramics and polymers. Throughout these classes, efficient thermoelectrics require good electronic properties (i.e. electrical conductivity and Seebeck coefficient - connected with the heat conversion capability), but low thermal conductivity κ. This is typically modelled as the sum of an electronic κ_e, and a lattice κ_L component, which represent the heat transported by charge carriers and lattice vibrations, respectively. As suppressing κ_e would adversely affect the electrical transport, optimization efforts need to focus on reducing κ through engineering κ_L. This requires a thorough understanding of the physical origin of a material's κ_L. In this regard, a powerful tool are elastic properties. Indeed, these can provide insights on a materials chemical bonding, which determines both the lattice capability of *carrying* vibrations (phonons), as well as, in part, its ability to *scatter* them.

The focus of the present review is to examine the elastic properties of thermoelectric materials. We will show how elastic constants behave for several classes of materials and how these can provide deep understanding of chemical bonding and thermal transport.

Elastic constants are a measure of a material's resistance to deformation under applied stress in the elastic regime[2,3] (i.e., sufficient stress to stretch chemical bonds, but not enough to break them). The term "constant" is a misnomer, however, since the elastic constants are not constant with respect to thermodynamic variables such as temperature[4] and pressure[5,6], or with respect to changes in composition or microstructure. From this point forward, we will refer to the elastic constants as elastic moduli. Though often dismissed as purely of interest for mechanical performance, elastic moduli are fundamentally connected to the chemical structure, and thus impact the transport physics in several important ways. Furthermore, they can be a useful probe of underlying structural and chemical changes in a material as a function of composition or temperature[7].

Thermoelectric materials have broadly varying elastic properties due to wide variations in chemical bonding. For example, stiff covalent bonds in tetrahedrally-bonded semiconductors (e.g., silicon) lead to much higher elastic moduli than the weaker secondary bonds in bulk polymers. This leads to marked disparities in transport properties – in particular phonon transport. Acoustic phonon velocities are determined directly from the elastic moduli, while the Grüneisen parameter, which determines phonon-phonon scattering rates, can be estimated from the temperature-dependence of the elastic moduli[8]. Elastic moduli also play a role in electronic transport by influencing electron-phonon scattering (i.e., acoustic deformation potential scattering[9,10]). Further, because elastic moduli are second-order derivatives of Gibb's free energy, temperature-dependent measurements serve as a powerful tool in the investigation and detection of both first- and second-order phase transitions[11]. Several important classes of thermoelectrics have phase transitions at high temperatures (e.g., SnSe[12–14], Cu_2Se[15,16], GeTe[17–20], kesterite and stannite[21–24], etc) and their elastic moduli can be used to reach a deeper understanding of the impact that structural changes have on transport properties. In the study of elasticity of functional materials, computation has far outpaced experiment, providing predicted elastic tensors for *thousands* of complex materials[25–28]. However, while Density Functional Theory (DFT) can easily yield single crystal elastic tensors in many cases, it cannot be readily applied to the study of phase transitions, to predict temperature-dependent behavior, or to study materials with high degree of disorder. Not to mention, the polycrystalline nature of most applied materials cannot be captured.

In the present review, our aim is to emphasize the importance of experimental elasticity measurements. We introduce the basic theory of elasticity, summarize the existing literature on temperature-dependent elastic moduli of thermoelectric materials, and discuss the value of such data in the investigation of thermal transport. Experimental approaches to measuring elastic moduli are presented, emphasizing high-temperature resonant ultrasound spectroscopy as an accurate yet simple tool. We conclude by discussing study cases from some of the authors, in which the determination of elastic moduli was decisive for interpreting the thermal transport behavior, as well as detecting changes in chemical bonding due to phase transitions.

2 Elastic moduli from a chemical bonding perspective

2.1 Elasticity basics

Definition of elastic moduli

The elastic moduli are a measure of a material's resistance to small (i.e., elastic) deformations under an applied stress[2,3]. Strain in the elastic regime is fully reversible because it does not involve any bond breaking or the formation or slip of dislocations. In this regime, Hooke's law relates stress, σ, to strain ε, by $\sigma = C\varepsilon$, where C is the elastic modulus, also known as the stiffness coefficient. Conversely, $\varepsilon = S\sigma$, where S is the compliance modulus. From a chemical bonding perspective, we can consider C and S as a measure of the stiffness (or softness) of the bonds in response to an applied stress. How stiff the bonds are in a crystal will determine a number of properties, including how lattice vibrations (phonons) propagate. Because crystalline materials are anisotropic, a tensor representation is needed to fully describe C and S. In this review, however, most of the discussion focuses on scalar values of the elastic moduli, which represent a polycrystalline average. Thus, readers need not be familiar with the tensor form. Nonetheless, we provide a brief introduction in section 2.2 for those interested in the physical interpretation of elastic tensors. A more comprehensive review of these concepts can be found in ref.[29,30].

Young's, bulk, and shear moduli

To calculate the response of a solid to an arbitrary stress state, one needs to use the full elastic tensor, represented by C_{ij}. However, for most purposes, we are only interested in a few specific types of stress: pure tensile stress along one axis, pure shear about one axis, or hydrostatic pressure. For these purposes, we rely on the "engineering elastic moduli": Young's modulus, shear modulus, and bulk modulus. These are shown schematically in Figure 1. The Young's modulus or modulus of elasticity, Y, is used to calculate the tensile strain ($\Delta l/l$) along the same axis as an applied tensile stress σ ($Y = \sigma(l/\Delta l)$). It is to be remembered that this and the following definitions are rigorous - and thus to be regarded - only in the limit of small displacements. The shear modulus, G, quantifies the shear strain ($\Delta w/l$) that results from a pure shear stress σ ($G = \sigma(l/\Delta w)$). The bulk modulus, B, measures the volume change ($\Delta V/V$) in response to a hydrostatic pressure P ($B = -P(V/\Delta V)$. Another useful quantity is the Poisson's ratio, μ, shown schematically in Figure 1, which is defined as ($\mu = (\Delta l/l)/(\Delta w/w)$), and illustrates the change in a materials cross section resulting from a change in length. It can also be defined as the ratio between the Young's and the shear moduli ($\mu = Y/2G - 1$). Perhaps surprisingly, μ can be used as an indicator of anharmonic bonding in a solid. We will return to this topic in section 4.5, when we discuss the ways in which elastic moduli can be used to estimate a material's Grüneisen parameter.

2.2 Elastic tensors

Crash course in single crystal elastic tensors

Describing an arbitrary stress or strain requires the use of 2^{nd} rank tensors represented by symmetric 3x3 matrices (Figure 2a-b). Due to the symmetry properties of these tensors, the 9 coefficients can be simplified to 6 independent terms (Figure 2b). The Voigt-notation representation of the applied stress, σ_i, is shown in Figure 2c. σ_1, σ_2, and σ_3 each describe a uniaxial stress (also known as tensile stress) along the x, y, or z axis, respectively. σ_4, σ_5, and σ_6 represent a shear stress about the x, y, or z axis, respectively. Likewise, the resulting strain, ε_j, can be either tensile (ε_1, ε_2, or ε_3) or shear (ε_4, ε_5, ε_6) in nature. The axes in Figure 2a correspond to the principal axes of the crystal system, as long as we are talking about systems with mutually perpendicular axes (cubic, tetragonal, orthorhombic). Thus, x points along the a-axis, y points along b, and z points along c. For hexagonal and trigonal crystal systems, z is aligned with the c-axis, and x is aligned with the a-axis. For lower symmetries, we refer the reader to ref.[29]. For most material design purposes, we need only to consider specific combinations of stress. For example, hydrostatic pressure (as used in diamond anvil cell experiments) means that $\sigma_1 = \sigma_2 = \sigma_3$, and $\sigma_4 = \sigma_5 = \sigma_6 = 0$. Or one might apply a uniaxial stress, as in tensile testing, such that σ_1 is positive, while $\sigma_{2-6} = 0$.

To describe the elastic response of a crystal, each of the 9 stress elements (Figure 2b) must be related to each of the analogous 9 strain elements. That makes a total of 81 coefficients. In tensor notation, C (or S) is thus represented as a 3x3x3x3 matrix of coefficients (*i.e.*, a 4^{th} rank tensor). Fortunately, symmetry considerations and the use of the Voigt notation allow C and S to be represented as “simple” 6x6 matrices (tensors). Thus, we can write $\sigma_i = \Sigma_j C_{ij} \varepsilon_j$, where i and $j = 1-6$ (Figure 2d). In single crystals, the number of non-zero, independent terms in the elastic tensor C_{ij} varies from just 3 for a cubic symmetry to 21 for a triclinic symmetry. A complete description and derivation of the elastic tensor elements for each crystal class can be found in ref.[29].

The elastic behavior of a single crystal must exhibit the same symmetry elements as the point group (Neumann's principle). For example, the Young's modulus of cubic PbTe and rhombohedral GeTe are shown in Figure 3 as a function of direction, using predicted elastic tensors from MaterialsProject.org[31]. In the rock salt compound, PbTe, the Young's modulus exhibits 4-fold rotational symmetry along the <100> directions, as well as 3-fold rotational symmetry along the <111> directions. The elastic response is the same along the three principal axes, but it is not isotropic. The <100> directions are significantly stiffer because they are directly aligned with the octahedral Pb-Te bonds. As expected, in rhombohedral GeTe, which has a distorted rock salt structure, the Young's modulus shows 3-fold roto-inversion symmetry about the <001> direction. Y is equal along the a- and b-axes, but not along the c-axis. The distortion of the octahedral environment in GeTe directly leads to the distortion of Y. However, Y is still stiffest approximately parallel to the Ge-Te bonds. The anisotropy in the elastic moduli of a single crystal will then be reflected in an analogous anisotropy of related material properties, such as sound velocities and lattice thermal conductivity.

Elastic moduli of polycrystalline materials

In the majority of experimental research on thermoelectric materials, we are dealing with bulk, polycrystalline samples. Assuming a polycrystalline sample has a statistically random grain orientation (*i.e.*, no texturing or preferred orientation), the elastic moduli will be isotropic and thus will be the related physical properties. This is illustrated by the spherical Young's modulus shown in Figure 3. The isotropic elastic tensor is fully described by just two independent terms: C_{11} and C_{44}. A third component, C_{12}, is related to the other two by $C_{12} = C_{11} - 2C_{44}$. In isotropic materials, C_{44} is equivalent to the shear modulus, G. C_{11}, however, is not directly equivalent to any engineering modulus (Y or B for example). However, if both C_{11} and C_{44} are known, converting to any of the engineering elastic moduli is straightforward. In fact, knowledge of any two of the moduli (C_{11}, C_{44}, G, Y, B, or μ) can be used to easily obtain any of the other ones using the relations summarized in Figure 4.

Effect of texturing

Experimentally, it is also common to encounter textured polycrystalline samples with strongly-oriented grains. This is more likely to occur for compounds with crystal structures characterized by highly anisotropic bond stiffness (e.g., Bi_2Te_3, SnSe, etc.). If texturing is the consequence of a uniaxial pressure during hot-pressing or spark plasma sintering (SPS), samples will likely acquire a transversely isotropic symmetry. In this case, the elastic tensor takes on the same symmetry as a hexagonal single crystal[32]. This means that the properties will be isotropic in all directions perpendicular (*i.e.*, transverse) to the applied pressure. Nevertheless, elastic constants in the direction parallel to the applied pressure may be either stiffer or softer than those along the transverse direction, depending on the preferred orientation. Most commonly, uniaxial pressing leads to grains preferentially oriented with the strongest bonds perpendicular to the application of pressure.

Elastic moduli from DFT calculations

Today, elastic tensors computed using density functional theory (DFT) are widely available, much more so than experimental

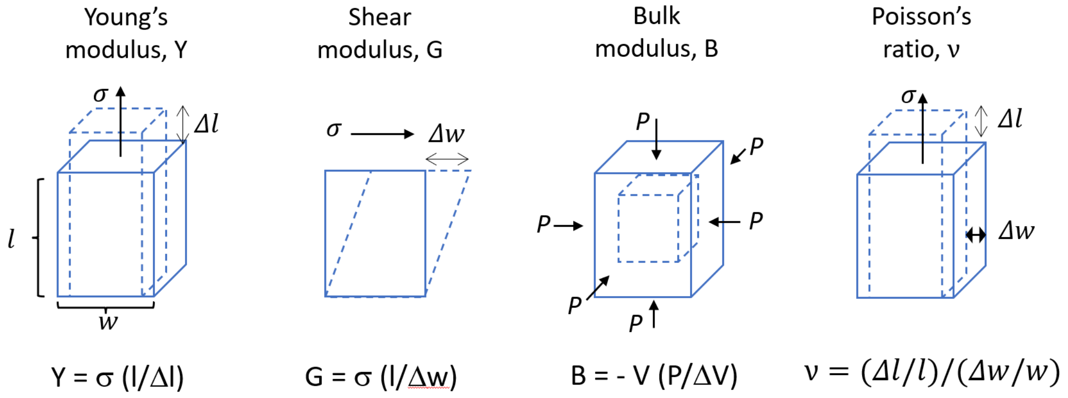

Fig. 1 Conceptual illustration of the "Engineering elastic moduli", so named because they describe simple stress states that are useful as material selection criteria. Formulas are intended in the limit of small displacements.

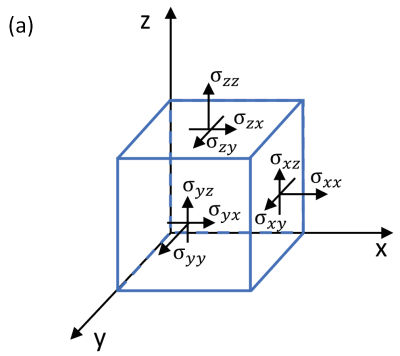

(b) Tensor notation

$$\begin{pmatrix} \sigma_{xx} & \sigma_{xy} & \sigma_{xz} \\ \sigma_{yx} & \sigma_{yy} & \sigma_{yz} \\ \sigma_{zx} & \sigma_{zy} & \sigma_{zz} \end{pmatrix} \xrightarrow[\text{symmetry}]{} = \begin{pmatrix} \sigma_1 & \sigma_6 & \sigma_5 \\ \sigma_6 & \sigma_2 & \sigma_4 \\ \sigma_5 & \sigma_4 & \sigma_3 \end{pmatrix} \longrightarrow$$

(c) Voigt notation

$$\begin{pmatrix} \sigma_1 \\ \sigma_2 \\ \sigma_3 \\ \sigma_4 \\ \sigma_5 \\ \sigma_6 \end{pmatrix}$$

(d)

$$\begin{pmatrix} \sigma_1 \\ \sigma_2 \\ \sigma_3 \\ \sigma_4 \\ \sigma_5 \\ \sigma_6 \end{pmatrix} = \begin{pmatrix} C_{11} & C_{12} & C_{13} & C_{14} & C_{15} & C_{16} \\ C_{21} & C_{22} & C_{23} & C_{24} & C_{25} & C_{26} \\ C_{31} & C_{32} & C_{33} & C_{34} & C_{35} & C_{36} \\ C_{41} & C_{42} & C_{43} & C_{44} & C_{45} & C_{46} \\ C_{51} & C_{52} & C_{53} & C_{54} & C_{55} & C_{56} \\ C_{61} & C_{62} & C_{63} & C_{64} & C_{65} & C_{66} \end{pmatrix} \begin{pmatrix} \varepsilon_1 \\ \varepsilon_2 \\ \varepsilon_3 \\ \varepsilon_4 \\ \varepsilon_5 \\ \varepsilon_6 \end{pmatrix}$$

Fig. 2 a) Illustration of the elements of the stress tensor. Each of the nine components is applied to one plane (identified by the normal), and points to a specific direction (e.g. σ_{ij}, for a stress applied on plane i and directed along j). b,c) Mathematical representation of the stress elements in the classical tensor notation (b) and in the Voigt notation (c), after symmetry considerations. The same illustration and mathematical formalism can be adopted for the strain tensor. d) Hooke's law relating stress and strain through the stiffness tensor represented in Voigt notation.

data. For the most part, calculated elastic tensors are accurate within 10-20% of experimental values[33]. A notable exception are compounds with van der Waals type of bonding, in which a standard DFT-based approach predicts in-plane elastic moduli with decent accuracy but tends to greatly underestimate out-of-plane elastic moduli. For example, in Bi_2Te_3, a 30% discrepancy is found between the DFT[33] and the experimental[34] C_{11}, while the calculated C_{33} is predicted more than five times lower than the experimental value. By its very nature, DFT is used to predict properties of single crystals. Usually, the full single crystal elastic tensor, C_{ij}, or compliance tensor, S_{ij}, is reported in the literature. For example, it is available for thousands of compounds on MaterialsProject.org[31]. It is important to note that the C_{11} and C_{44} terms of the single crystal tensor obtained from DFT cannot be directly used as a proxy for the "isotropic" C_{11} and C_{44} values of a hypothetical polycrystal of the same material. However, it is possible to convert from the single crystals tensor to an isotropic tensor using an averaging scheme. Two different averages – an upper bound (Voigt) and a lower bound (Reuss) - are typically used to estimate the engineering elastic moduli (B, Y, G) of a polycrystal from the single crystal elastic tensor. The average of the upper and lower bounds (an average of two averages) is often taken as the best estimate for the polycrystal. This averaging procedure is known as the Voigt–Reuss–Hill method and can be found in ref[33]. Note that once you calculate B, Y, and G of the polycrystal, you can convert to the respective C_{11} and C_{44} using Figure 4. It's important to keep in mind that the Voigt–Reuss–Hill averaging scheme does not account for local changes (most likely softening) in the elastic moduli that may be caused by grain boundaries (see section 2.3). The assumption inherent in the Reuss and Voigt approximations is that the strain and disorder at grain boundaries have no effect on the elasticity of the crystalline phase.

2.3 Structure-property relations

Elastic moduli and composition

The elastic moduli are a measure of bond stiffness, which in turn is a strong function of bond length. In covalent bonds, increased orbital overlap can be seen as responsible for stiffer bonds. In ionic materials, the same is caused by increased coulombic attraction. Regardless of the ionic or covalent character, one will find that the elastic moduli (e.g., Y, B, G) tend to decrease smoothly as a function of average bond length within any single class of isostructural materials[29,35]. Within the same material, stiffness can vary up to an order of magnitude along different crystallographic directions, again correlated with bond length

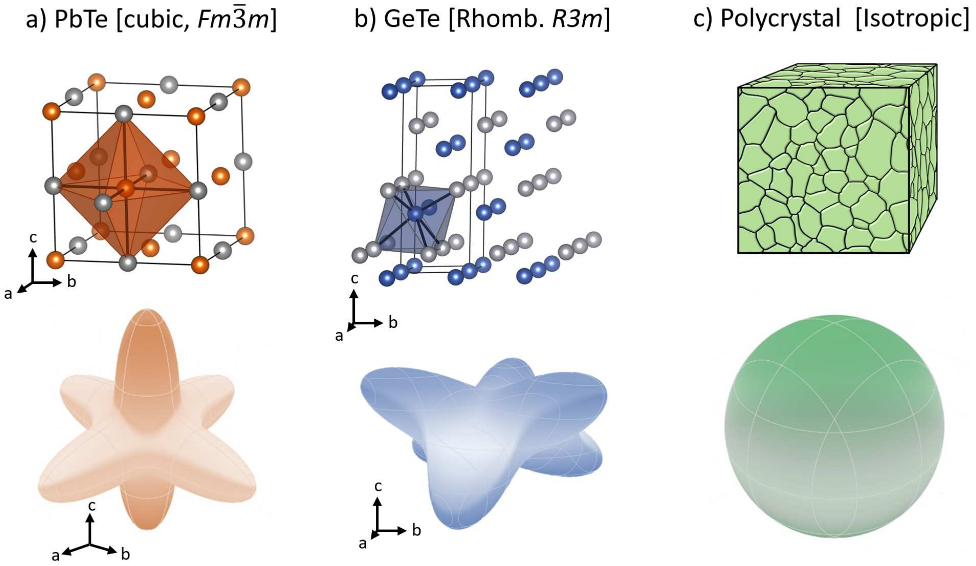

Fig. 3 Upper row: crystal structures for cubic rock-salt PbTe and rhombohedral distorted rock-salt GeTe, and an isotropic polycrystal. Lower row: The isosurfaces show the magnitude of the Young's modulus as a function of crystallographic direction for a cubic, rhombohedral, and isotropic materials. Even in a cubic material, the elastic moduli are anisotropic. In the case of rock salt chalcogenides, single crystals are much stiffer along the $< 100 >$ family of directions than along $< 111 >$. Elastic tensors from MaterialsProject.org[31].

		Elastic moduli for isotropic solids			
		Bulk modulus *(B)*	Young's modulus *(Y)*	Shear modulus *(G)*	Poisson's ratio *(μ)*
known elastic moduli	*(B, Y)*	-	-	$\frac{3YB}{9B-Y}$	$\frac{3B-Y}{6B}$
	(B, G)	-	$\frac{9BG}{3B+G}$	-	$\frac{3B-2G}{2(3B+G)}$
	(B, μ)	-	$3B(1\text{-}2\mu)$	$\frac{3B\,(1-2\mu)}{2\,(1+\mu)}$	-
	(Y, G)	$\frac{YG}{3(3G-Y)}$	-	-	$\frac{Y}{2G}-1$
	(Y, μ)	$\frac{Y}{3(1-2\mu)}$	-	$\frac{Y}{2\,(1+\mu)}$	-
	(G, μ)	$\frac{2G\,(1+\mu)}{3\,(1-2\mu)}$	$2G(1+\mu)$	-	-
	(C_{11}, C_{44})	$C_{11}\text{-}\frac{4}{3}C_{44}$	$\frac{C_{44}(3C_{11}-4C_{44})}{C_{11}-C_{44}}$	C_{44}	$\frac{\frac{C_{11}}{2}-C_{44}}{C_{11}-C_{44}}$

Fig. 4 Formulas summarizing the relationship among elastic moduli. The knowledge of any two moduli allows the calculation of all the others.

and stiffness (e.g., graphite presents a 23-fold higher C_{11} than C_{33}, reflecting the anisotropy between strong in plane covalent bonds, and weak out of plane inter-layer bonding). This has been shown in countless papers and is often discussed in the introductory chapters of materials science and solid-state chemistry textbooks[29]. In materials comprised of primary bonds and weak interactions (e.g., polymers, graphite), the elastic moduli can be highly dependent on crystallinity and the orientation of the covalent bonds. Stiffness, represented here in terms of the Young's modulus, varies from 1150 GPa for diamond[36] to 1 GPa for a polymer like PEDOT:PSS[37], and this entire spectrum is entirely a result of differences in chemical bonding. Outliers to the "longer-corresponding-to-softer-bonds" trend are rare, thus worth a second look. In section 5.1, we will discuss the special case of Mg_3Sb_2, which is softer than isostructural compounds with larger unit cells.

Effect of microstructure

Compared with the mechanical properties that involve plastic deformation (e.g., hardness, yield and ultimate strength, toughness), the elastic moduli are less sensitive to microstructural changes. However, microstructure introducing a large degree of strain into a sample can have an impact on elastic moduli. Common causes of micro-strain in a sample are dislocations, stacking faults, and twinning. Locally, strain leads to softer (more compliant) bonds. If the density of such defects is high (e.g., induced by high-energy ball-milling), one can observe softening of the overall elastic moduli of the sample. This has been shown recently in PbTe, where the introduction of microstrain through dislocations was shown to have a direct correlation with softening, identified in a decrease of sound velocity (and thus of lattice thermal conductivity)[38,39]. Similarly, elastic moduli can be a function of grain size. Samples with large grains ($> 10\mu m$), in which grain boundaries themselves make up a negligible volume fraction of the bulk material, should basically have the same overall elastic moduli as the single crystalline average (see discussion of Reuss, Voigt, Hill averages in section 2.2). However, at the limit of nanograined samples, the highly strained grain boundaries will lead to an overall softening of the elastic moduli. To this end grain boundaries can be treated as a separate phase, softer than the bulk[40,41].

3 Temperature dependence of elastic moduli

3.1 Softening of elastic moduli with temperature

The elastic moduli of most solids decrease with increasing temperature until the melting point. Although if compared to other material properties the variation is relatively weak, over a wide temperature range it can be significant enough (up to 30%) that it should be accounted for when modeling the thermal and mechanical behavior. The decrease in elastic moduli, or softening, arises from the 3^{rd} and higher-order terms in the interatomic potential energy, given by $V(r) = V(0) + a_2(r - r_0)^2 + a_3(r - r_0)^3 + a_4(r - r_0)^4 ...$, where $r - r_0$ is the displacement of an atom from its equilibrium position, a_2 is the magnitude of the harmonic term, and a_i (i>2) represent the anharmonic terms. Each element of the elastic tensor, C_{ij}, can have its own temperature dependence, owing to the stretching or shearing of bonds along different crystallographic directions. Here, we will focus on the temperature dependence of the Young's modulus. In fact, Y is related to the curvature at the vertex of the interatomic potential as $Y = \frac{1}{r_0}\left(\frac{\partial^2 V}{\partial r^2}\right)_{r=r_0}$. A larger curvature corresponds to a narrower potential well and thus stiffer bonds. In a completely harmonic potential, the curvature is energy-independent, implying a constant Y as a function of temperature. Nevertheless, the interatomic potential of real solids inevitably contains anharmonic terms, which leads to decreasing Y with temperature. Importantly, the temperature derivative of elastic moduli is a useful measure of the anharmonic contribution to bonding, quantified by the Grüneisen parameter, γ (further discussion and formal definition in section 4.5). Below, we will describe thermodynamic models that relate the thermodynamic γ to the temperature-dependence of elastic moduli, review relevant experimental techniques for their determination, and then discuss the trends found in the temperature-dependent moduli of thermoelectric materials.

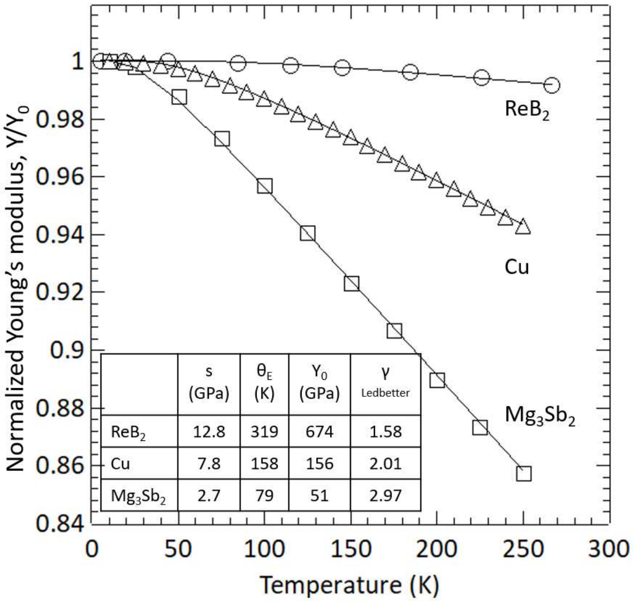

	s (GPa)	θ$_E$ (K)	Y$_0$ (GPa)	γ Ledbetter
ReB$_2$	12.8	319	674	1.58
Cu	7.8	158	156	2.01
Mg$_3$Sb$_2$	2.7	79	51	2.97

Fig. 5 Young's modulus, normalized to the fitted 0 K value, as a function of temperature for solids ranging from soft and anharmonic (Mg_3Sb_2) to stiff and harmonic (ReB_2)[32,42]. The solid curves are fit using Eq. 1, where θ_E is related to the Einstein temperature, s is a fitting parameter related to the slope, Y_0 is the Young's modulus at 0 K. The Grüneisen parameter, $\gamma_{Ledbetter}$, was obtained by fitting the linear portion of the slope with Eq. 2.

Fig.5 illustrates the typical behavior of Y as a function of temperature. Here, we employ the normalized Y/Y_o to enable a comparison of materials (ReB_2[32], Cu[43], and Mg_3Sb_2[42]) with significantly different 0 K Young's modulus, Y_o. At very low temperature, it is typical for elastic moduli to plateau at a constant value, reflecting the harmonic curvature of the bottom of the interatomic potential. As temperature increases, the elastic moduli typically decrease linearly, provided that no phase transition occurs within the measured temperature range. In 1970, Varshni[44] put forward an expression based on the Einstein-oscillator model to describe the temperature-dependence of any elastic modulus, C_{ij}:

$$C_{ij} = C_{ij}^0 - \frac{s}{e^{\theta_E/T} - 1}. \tag{1}$$

Here, C_{ij}^0 denotes the elastic modulus at 0 K, θ_E is related to the Einstein temperature, and s is a fitting parameter that represents the curvature of the transition region. The solid curves in Fig. 5 show that the Varshni equation provides an excellent fit for for ReB_2, Cu, and Mg_3Sb_2. In fact, for most solids Eq. 1 has proven to be the best representation of the low- and mid-temperature trends of elastic moduli. In the higher temperature linear regime, an expression derived from the Varshni equation (Eq. 1) by Ledbetter et Al. can be used to estimate the Grüneisen parameter[45].

$$\frac{dY}{dT} = -\frac{s}{\theta_E} = -\frac{3k\gamma(\gamma+1)}{V_a}, \tag{2}$$

where dY/dT is the slope of the Young's modulus with respect to temperature, γ is the Ledbetter Grüneisen parameter, k is the Boltzmann constant, and V_a is the volume per atom. Note that the original formulation reported in ref[45] is expressed for dB/dT. In principle, an estimate of the Grüneisen parameter can be obtained from the temperature derivative of any elastic modulus. As it will be further discussed in section 4.5, the estimate will inevitably depend on the used modulus. In this case, we employed dY/dT as one of the most widely available properties. By fitting the high temperature slope with Eq. 2 we obtain the estimates for γ shown in Fig. 5. Alternative methods to calculate γ will be discussed in section 4.5. To differentiate between them, we refer to this estimate as $\gamma_{Ledbetter}$.

3.2 Measurement techniques

It is worthwhile at this point to briefly discuss methods used to measure elastic moduli at high temperature. The most common technique for room temperature sound velocities (directly related with elastic moduli, as it will be described in section 4.2), is ultrasonic time-of-flight, or pulse-echo ultrasound, measurements[46,47]. The speed of sound is quantified by measuring the time it takes for an acoustic pulse to travel across a known length of the sample. The most common setups are (i) the double-transducer one, where a piezoelectric transducer emits a wave packet and the transit time is acquired by a pickup transducer positioned at the opposite side of the sample; (ii) the single-transducer setup, where the pulse-echo time (to the opposite face of the sample and back to the emitter) is recorded. More details on this method can be found in ref.[46]. Pulse-echo ultrasound measurements provides uncertainties in the order of 1%, are not very demanding in terms of sample geometry, the data analysis is straightforward, and the equipment is accessible. However, the method typically requires a relatively large sample (e.g. 5x5x1 mm^3), and different measurements are needed to obtain independent elastic moduli. The main disadvantage though is with respect to temperature-dependent acquisitions. In fact, a coupling medium (typically a gel with the consistency of honey) is required between the sample and the transducers, and often the sample needs to be re-mounted to obtain an adequate signal. Therefore, it is challenging to design an enclosed atmosphere- and temperature-controlled apparatus for low or high temperature data collections.

Resonant ultrasound spectroscopy (RUS) is the most accurate technique to determine the elastic moduli of solids[7,48,49]. This is the method employed for most of the temperature-dependent data in this article. During the measurement, the sample is lightly-clamped on diagonal corners between two piezoelectric transducers. The emitter generates a signal over a wide range of vibrational frequencies, while the pickup transducer collects the sample response[7,48]. Resonance peaks can be observed when the excitation frequency matches the Eigen-frequency of the sample. Conceptually, each resonant peak can be viewed as the frequency of one low energy acoustic phonon mode of the sample. The temperature-dependence of a peak frequency is thus a measure of the anharmonic character of a specific phonon mode. The elastic tensor of the sample is obtained by iteratively matching the observed resonant frequencies with calculated ones using widely-available open-source software[50]. Although in principle resonances from any sample geometry can be predicted and measured, this process is most feasible when using well-defined ones such as parallelepipeds, cylinders, or spheres[7,51,52]. For polycrystalline samples, C_{11} and C_{44} are obtained in a unique measurement. For single crystals, all the tensor elements can be obtained in a single measurement, though the analysis is increasingly challenging (higher number of unknown variables), especially if the sample is not properly cut and oriented. Further, the attenuation or damping of individual acoustic phonons can be determined with RUS, as this is inversely proportional to the peak quality factor (based on the full-width at half-maximum)[53]. Since RUS yields a complete set of elastic moduli from a single scan, eliminating the need of remounting, it results being convenient for measurements under varying temperature or atmospheric conditions. In addition, the absence of a coupling medium eliminates issues with thermal expansion mismatches and sublimation or reactivity of the couplant, enabling to carry out measurements under extreme temperatures[48].

Other techniques are also available. Mechanical methods, such as tensile, compression, and micro-hardness tests, can be used for a direct determination of elastic moduli. These are typically destructive, and most often used for ductile specimens such as metals and composites. Diffraction and scattering techniques including Brillouin scattering[54–56], X-ray residual strain analysis[57], high-pressure X-ray diffraction[58], and inelastic neutron scattering[59,60], can yield an indirect measurement of moduli. These require specialized equipment and are not designed specifically for elastic moduli. Acoustic methods result therefore being particularly advantageous, as non-destructive and more accurate than mechanical methods, as well as more readily available than most scattering or diffraction-based techniques.

3.3 Temperature-dependent moduli of thermoelectric materials

In Fig. 6, we have compiled selected high-temperature Young's modulus data for various classes of thermoelectric materials. Most of the data were measured on bulk polycrystalline specimens using RUS. Although the availability of high-temperature elastic constants for thermoelectric materials remains quite limited, Fig. 6 still illustrates the wide range of elastic stiffness among different classes. Half-Heuslers and $Si_{1-x}Ge_x$ are among the stiffest thermoelectrics, due to their short, stiff covalent bonds. Similarly, clathrates are relatively stiff, as a result of the covalently bonded cage-like structures. In general, compounds with octahedral coordination, (e.g., rock-salt compounds SnTe and PbTe) are softer than those with tetrahedral coordination (half Heuslers). In the case of AM_2X_2 Zintls, the alternating layers of tetrahedral and octahedral coordination may explain their intermediate values of Y.

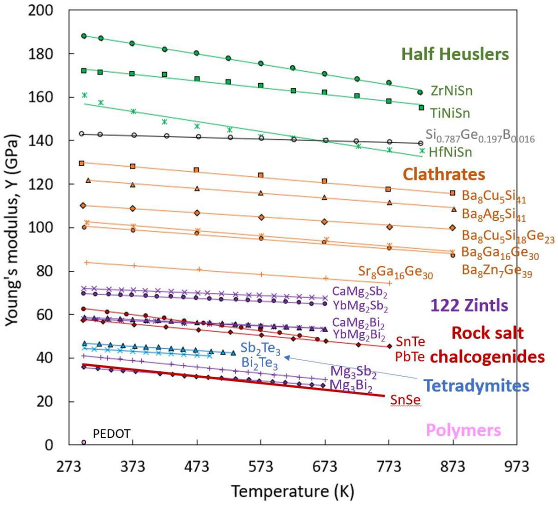

Fig. 6 Temperature-dependence of the Young's modulus, Y, of selected thermoelectric materials[37,48,61–71]. Half-Heuslers and $Si_{1-x}Ge_x$ are among the stiffest thermoelectric materials due to their short covalent bonds. The softest crystalline materials are the layered tetradymites and Mg_3Sb_2 and Mg_3Bi_2. At the lower left corner, PEDOT, an extremely soft conducting polymer, is shown for comparison.

The softest crystalline materials shown in Fig 6 are the tetradymites (Sb_2Te_3 and Bi_2Te_3), which have structures that combine covalent octahedral layers with van der Waals bonding, SnSe, possessing a layered structure with soft in plane accordion-like bonds[72], and Mg_3Sb_2 and Mg_3Bi_2, which exhibit anomalously low shear moduli and will be discussed further below. Finally, the extremely low Young's modulus of a typical conducting polymer, PEDOT:PSS, is shown for comparison.

Fig. 6 also emphasizes the dual roles of structure and composition in determining the magnitude of Y. Within the same structure type, differences in atomic radii often determine the stiffness of individual compounds. For example, the Ge-based clathrates are generally softer than Si-based clathrates, and among AM_2X_2 Zintls, the Bi-based compounds are generally softer than Sb-analogues due to the larger size of Bi. Nevertheless, composition does not strongly impact the temperature slope of moduli, and thus the anharmonicity. The exact values of elastic moduli and softening rate can be found in Supplemental Table 1. The difference in Y explains much of the difference in lattice thermal conductivity across materials. For example, Half Heuslers' κ_L is inherently high due to their high bond stiffness. In particular, ZrNiSn has a κ_L of 17.2 W/mK at room temperature[73], which is on the high end of thermoelectric materials. PEDOT, on the other hand, is a class of conducting polymer with inherently ultra-low κ ($\sim$ 0.4 - 0.9 W/mK)[74]. The Young's modulus of PEDOT thin films, as shown in Fig. 6, is typically around 1 GPa[37,68,69].

To highlight the relative softening rate of different material classes, Fig. 7 shows the fractional change in Y with respect to the room temperature value. While the modulus of $Si_{1-x}Ge_x$ only decreases by 3% between 300 and 900 K, traditional thermoelectrics, such as PbTe and SnTe soften by as much as 20% within their operational temperature range (approximately 300-700 K). As a general trend, materials with lower melting temperatures, T_M, are expected to exhibit a more rapid decrease of Y with temperature. For example, PbTe has T_M = 1197 K, while $Si_{0.8}Ge_{0.2}$ has T_M = 1623 K. The compounds Mg_3Sb_2 and Mg_3Bi_2, with T_M of 1698 K[75] and 1093 K[76], respectively, defy this trend. The origin of this behavior is discussed in section 5.1.

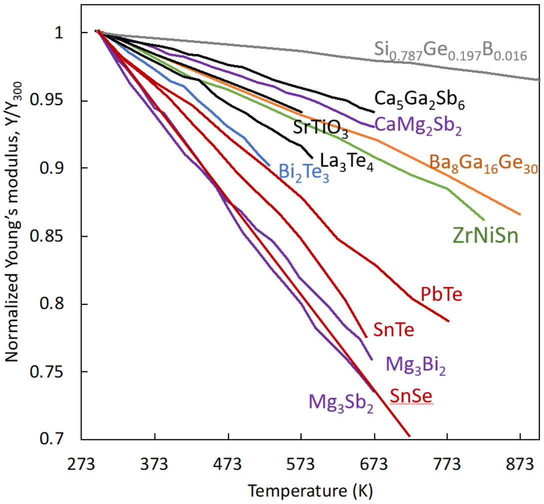

Fig. 7 Temperature-dependence of the Young's modulus normalized to the room temperature value, Y/Y_{300}. Large disparities in the relative rate of softening are found among different compounds.[48,61–67,77]

.

4 Elastic moduli as predictors of lattice thermal conductivity

4.1 Overview

For semiconductors, the dominant carriers of heat are charge carriers and lattice vibrations, which are responsible for κ_e and κ_L, the electronic and lattice components of thermal conductivity, respectively[78]. Lattice vibrations in a solid, or phonons, can be broadly grouped into two categories: high frequency optical modes involving opposing vibrations of atoms, and lower frequency acoustic modes in which neighboring atoms move concurrently. For this last category the group velocity, or sound velocity, is directly related to the elastic moduli. Although this is not always the case and should not be taken for granted[79–82], in most materials acoustic phonons dominate the heat transport[78,83]. Hence, a widely used approximation for the lattice thermal conductivity, derived from the kinetic gas model, is given by:

$$\kappa_L = \frac{1}{3} C_v v_{sound}^2 \tau. \tag{3}$$

Here, κ_L is proportional to the specific heat C_v, sound velocity v_{sound}, and phonon relaxation time τ[84]. Compared with the inherent nature of C_v, v_{sound} and τ can be more readily controlled and are therefore the focus of most optimization studies of thermoelectric materials. As it will be discussed below, quantification and trends of both v_{sound} and τ can be obtained from measurements of elastic moduli.

4.2 Determining sound velocities from elastic moduli

Sound velocities represent the speed at which low frequency lattice vibrations travel in a solid. In phonon dispersion relations, they are identified as the slope of the acoustic branches as frequency approaches zero. From equation 3, we can readily infer how v_{sound} represents a main contributing factor to thermal transport. Indeed, it is the greatest contribution to variations in κ_L between different classes of materials. For example, stiff covalent bonds in tetrahedrally-coordinated crystals yield several magnitudes larger sound velocities than weakly bonded polymers (diamond average v_{sound} $\sim$14000 m/s[85], PEDOT:PSS $\sim$900-1400 m/s[86]), contributing to the marked deviations in κ_L (diamond $\sim$2000 W/mK[87], PEDOT:PSS $\sim$0.4-0.9 W/mK[86]). The sound velocity is proportional to the square root of the elastic moduli and inversely proportional to the square root of density ρ ($v_{sound} \propto \sqrt{C/\rho}$). Therefore, measuring the elastic moduli of a solid is the most accurate approach to measuring its speed of sound, as the two properties are related via only one, easily-quantifiable parameter, *i.e.* density.

Isotropic solids

As discussed in section 2.2, the form of the elastic moduli tensor is strictly dependent on the crystal symmetry of a solid. Consequently, sound velocities preserve this dependence. In isotropic polycrystalline samples the behavior is not dependent on the crystal class. In this case, the longitudinal sound velocity, v_L, and the shear sound velocity, v_s are given by Eq. 4 and Eq. 5, in which B is the bulk modulus, and G is the shear modulus. Eq. 6 can be used to estimate an average or effective sound velocity $v_{sound,m}$.

$$v_L = \sqrt{\frac{B + \frac{4}{3}G}{\rho}} \tag{4}$$

$$v_s = \sqrt{\frac{G}{\rho}} \tag{5}$$

$$v_{sound,m} = \left[\frac{1}{3} \left(\frac{1}{v_L^3} + \frac{2}{v_s^3} \right) \right]^{-\frac{1}{3}} \tag{6}$$

Eq.s 4 and 5 explain why many of the best thermoelectric materials contain large, heavy elements: these often lead to high density and soft bonds, both of which cause low sound velocities and thus a suppression of lattice thermal conductivity. Note that soft bonds do not necessarily mean a mechanically weak sample. In fact, softer bonds are often associated with materials that are less prone to brittle failure and more likely to exhibit ductile behavior, which is more favorable for practical applications[88]. Since sound velocities can be readily obtained from ultrasonic measurements or first-principles calculations, they are the primary factor that should be considered when evaluating trends in lattice thermal conductivity across a series of materials. In particular, when κ_L, C_v and v_{sound} are all known, differences in the phonon scattering rate can be evaluated (see Eq. 3).

Single crystals

In non-isotropic materials (*i.e.* single crystals or strongly textured polycrystalline samples), the sound velocities are dependent on the crystal class and direction propagation. It is to be noted that only for certain crystallographic directions the propagating wave produces pure transversal or longitudinal modes[89]. For such cases, the relationships between C_{ij} and sound velocities for different crystal classes can be found in ref.[90,91]. Generalized relationships including non-pure modes require solving the Christoffel equation. Useful calculation tools can be found in ref.[89,92,93]. As an example, Table 1a shows the experimental elastic moduli for trigonal Bi_2Te_3[94,95]. The anisotropic form of the tensor produces a marked contrast in sound velocities along different crystallographic directions, as reported in Table 1b (only pure modes are considered). The anisotropy in elastic moduli, and thus in sound velocities, explains the anisotropy in κ_L[93]. An illustration of the concepts of wave propagation and polarization in a crystal is presented in Figure 8.

4.3 Debye-Callaway model

Eq. 3 represents a simplified picture of lattice thermal conductivity, where the frequency dependence of each term is neglected. This can allow for quick estimates but often fails in capturing the whole experimental behavior of materials. A commonly used approach is the Debye-Callaway model[96]. According to the Boltzmann transport theory of phonons, the frequency-dependent κ_L can be expressed by Eq 7, where is ω the phonon frequency and v_g is the group velocity.

$$\kappa_L = \frac{1}{3} \int_0^{\omega_{max}} C_V(\omega) v_g(\omega)^2 \tau(\omega) d\omega \tag{7}$$

From here, three main assumptions are typically introduced[84]. The first approximation relies on the Debye model of the phonon dispersion relation. This assumes the phonon group velocity as frequency-independent and equal to the low frequency limit, *i.e.*v_{sound}. The effective sound velocity (Eq. 6) can further be used for v_{sound} to capture a transversal and longitudinal mode-averaged behavior. Second, the high temperature limit for the heat capacity is used, which is sufficiently accurate for materials above their Debye temperature. Finally, Umklapp or phonon-phonon scattering is considered as the dominant contribution to τ. This means that other phonon scattering mechanisms, otherwise accounted for as series contributions to the overall τ ($\tau^{-1} = \Sigma_i \tau_i^{-1}$), are neglected. This is acceptable for non-heavily nanostructured and non-doped materials, when point defect and boundary scattering are not dominating the phonon behavior.

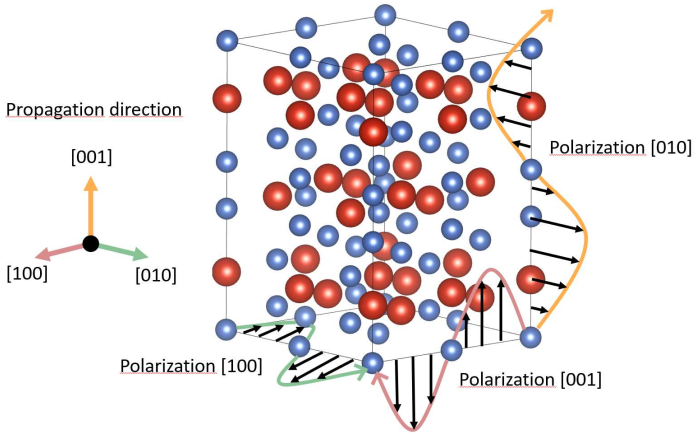

Fig. 8 Bi_2Te_3 crystal structure with cartoon explaining wave propagation and polarization. A wave with propagation direction [100] and polarization [001], one with propagation direction [010] and polarization [100] and one with propagation direction [001] and polarization [010] are illustrated.

Overall, this model yields a description of κ_L expressed by Eq. 8, where $\bar{M}$ and $\bar{V}$ are the average mass and volume per unit atom, γ is the Grüneisen parameter, and T is the absolute temperature. A full derivation can be found in ref.[84].

$$\kappa_L = \frac{(6\pi^2)^{2/3}}{4\pi^2} \frac{\bar{M} v_{sound}^3}{\bar{V}^{2/3} \gamma^2 T} \tag{8}$$

The adoption of this formalism allows to use the speed of sound to describe the overall acoustic phonon behavior of a material. This results particularly convenient as v_{sound} can be readily obtained either from direct measurements, or from the elastic moduli (experimental or calculated) with Eqs. 4-6. It is to be noted that Eq. 8 neglects the contribution of optical modes to phonon transport. In the case of simple materials, most of the heat is carried by acoustic phonons, and Eq. 8 results sufficiently accurate. For complex compounds with a large crystal structure[97] the contribution of higher-frequency optical modes becomes relevant. In these cases, a correction to Eq. 8 can be applied to take into account the optical contribution, and can be found in refs.[84,97].

This model has been demonstrated to perform well, predicting κ_L within a factor of two when experimental values are used for v_{sound} and γ[84]. When unavailable, the model still was able to yield surprisingly good predictions. Indeed, for classes of materials with lattice thermal conductivity spanning across four orders of magnitude, the model was able to predict κ_L within one or-

a) $$C_{ij} = \begin{bmatrix} 68.47 & 21.77 & 27.03 & 13.25 & 0 & 0 \\ 21.77 & 68.47 & 27.03 & -13.25 & 0 & 0 \\ 27.03 & 27.03 & 47.68 & 0 & 0 & 0 \\ 13.25 & -13.25 & 0 & 27.38 & 0 & 0 \\ 0 & 0 & 0 & 0 & 27.38 & 13.25 \\ 0 & 0 & 0 & 0 & 13.25 & 23.35 \end{bmatrix}$$

b)

Propagation direction	**Anisotropic sound velocity**
[100]	Polarization [100] $v_L = \sqrt{C_{11}/\rho} = 3028$ m/s
	Polarization [010] $v_{T1} = \sqrt{\frac{1}{2}(C_{66}+C_{44}-((C_{44}-C_{66})^2+4C_{14}^2)^{\frac{1}{2}})/\rho} = 2278$ m/s
	Polarization [001] $v_{T2} = \sqrt{\frac{1}{2}(C_{66}+C_{44}+((C_{44}-C_{66})^2+4C_{14}^2)^{\frac{1}{2}})/\rho} = 1265$ m/s
[001]	Polarization [001] $v_L = \sqrt{C_{33}/\rho} = 2526$ m/s
	Polarization [100] and [010] $v_L = \sqrt{C_{44}/\rho} = 1915$ m/s

Table 1 (a) Experimental elastic moduli tensor for trigonal Bi_2Te_3, with values in GPa. The anisotropic form of the tensor leads to anisotropy in the speed of sound, calculated in panel (b) for purely transversal or longitudinal modes, and thus in lattice thermal conductivity. Density $\rho = 7.47$ g/cm^3.

der of magnitude of the experimental value[98], further dropping the accuracy to within 1.5 when a correction for anharmonicity was employed[99]. An extension of the model to account for the anisotropy in the lattice thermal conductivity of crystals was also successfully tested[93]. These studies are making use of DFT moduli to calculate the sound velocity. For most compounds, these can be found at MaterialsProject.org[31], allowing quick and accessible predictions.

4.4 Temperature dependence of speed of sound

As explained in the previous sections, elastic moduli present a dependence over temperature which is reflected in temperature-dependent sound velocities. The Debye-Callaway model is derived assuming a constant cell volume, which implies no changes in heat capacity due to thermal expansion and constant sound velocities. Therefore, κ_L predictions based on the Debye-Callaway model usually limit the temperature dependence to the phonon scattering time term only, employing constant values for v_{sound}. This can lead to systematic inaccuracies when compared to experiments. In fact, since κ_L is proportional to the cube of sound velocity, deviations in the latter can propagate considerably to the former. For example, using room temperature experimental values of v_{sound} for PbTe[100] leads to a 9% overestimate of sound velocity at 700K, causing a 25% overestimation of κ_L with respect to calculations employing the experimental temperature-dependent v_{sound}. However, if a constant C_p is used (Doulong-Petit limit), these errors tend to cancel out, as the experimental C_p instead increases with temperature due to thermal expansion. Figure 9a shows the relative variation of experimental v_{sound} and C_p for PbTe (data from refs.[100,101]). Figure 9b illustrates instead the result of applying constant or temperature-depended v_{sound} and C_p to the Debye-Callaway model. Despite the partially compensating trends of v_{sound} and C_p over temperature, discrepancies in the models can still be observed. This further motivates the advantage of employing temperature-dependent experimental sound velocities: it can improve the accuracy of existing models, overall leading to improved understanding for established materials and better predictions for novel compounds. This can be particularly relevant for materials with predicted large anharmonicity, where a heavy dependence of v_{sound} and C_p with temperature is expected.

4.5 A comparison of Grüneisen parameter estimates

In addition to yielding v_{sound}, elasticity measurements can provide relevant information on the relaxation time of acoustic phonons. As discussed in section 3.1, the rate of softening of a material (*i.e.*, dY/dT) is directly related to the degree of bond anharmonicity, quantified by the Grüneisen parameter, γ. Being able to accurately estimate γ is important to gain insights on the Umklapp or phonon-phonon scattering rate τ_U, as $\tau_U \propto 1/(T\gamma^2)$. The same dependence is then carried on κ_L (Eq. 8). Although Umklapp is not always the dominant scattering mechanism in thermoelectrics (point-defect and boundary scattering also play an important role), it becomes increasingly important in all solids at high temperature, and it is the only scattering mechanism that occurs even in a perfect, defect-free crystal. Unfortunately, there is no single approach to estimate γ. From a microscopic perspective, each vibrational mode has its unique mode Grüneisen parameter γ_i, expressed as

$$\gamma_i = -\frac{\partial ln\omega_i}{\partial lnV}, \qquad (9)$$

in which ω_i is the vibrational frequency of the phonon mode i, and i is the unit cell volume.[102] Note that γ_i can take on either negative or positive values, both related to anharmonic behaviors. A mean Grüneisen parameter can be obtained by taking an average of the mode Grüneisen parameters weighted on the heat capacity of each vibrational mode $C_{V,i}$, as $\gamma = \frac{\sum_i \gamma_i C_{V,i}}{\sum_i C_{V,i}}$. Even though it is straightforward to obtain γ_i for all phonons from DFT calcu-

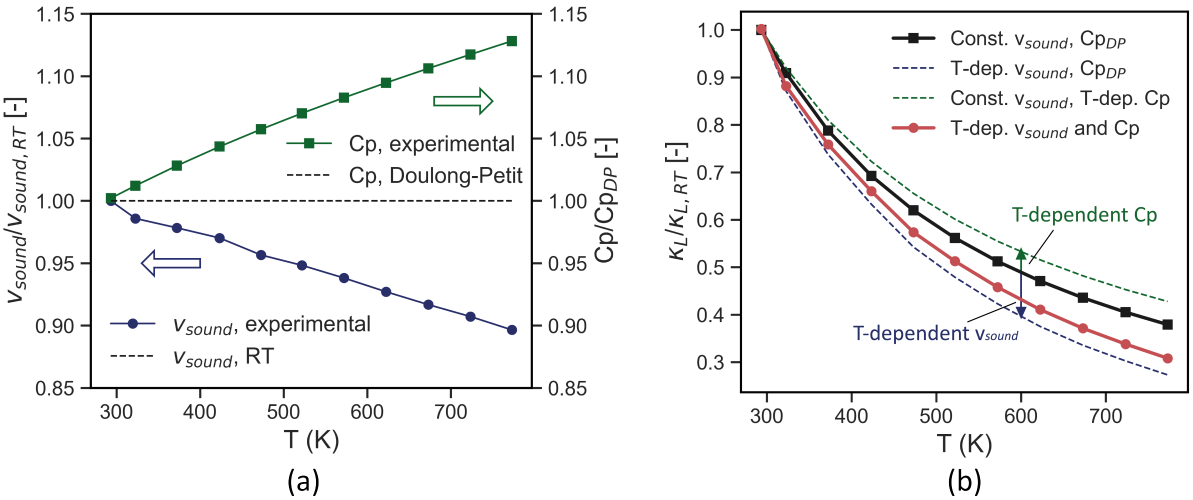

Fig. 9 (a) Relative variation of experimental sound velocity and heat capacity at constant pressure for PbTe (data from refs.[100,101]). Normalization is with respect to the room temperature sound velocity and the Doulong-Petit limit for heat capacity, respectively. b) Lattice thermal conductivity calculated from the Debye-Callaway model for PbTe, assuming Umklapp-dominated phonon scattering. Employing constant (room temperature v_{sound} and Doulong-Petit C_p) or temperature dependent (experimental) parameters causes deviations in the temperature trend. Values are normalized with respect to room temperature calculations.

.

lations, it is prohibitively difficult experimentally. For example, γ_i for arbitrary modes can be painstakingly extracted from single crystal neutron scattering measurements and γ_i for specific zone center modes can be obtained from Raman spectroscopy[103,104]. However, the complete experimental determination of γ_i for complex solids remains out of reach. For this reason, reported experimental Grüneisen parameters are usually a thermodynamic, or "average" γ, obtained from more accessible properties such as thermal expansion or elastic moduli. Here we show some of the employed methods.

4.5.1 Temperature dependence of elastic moduli

As described in section 3.1 (Eq. 2), we can directly obtain the Grüneisen parameter, $\gamma_{Ledbetter}$, of a material from the temperature derivative of elastic moduli. Specifically, $\gamma_{Ledbetter}$ should be considered an estimate of the anharmonicity of acoustic phonon modes. In Fig. 10, Eq. 2 is used to estimate $\gamma_{Ledbetter}$ for a variety of thermoelectric materials and traditional semiconductors. Here, the Bulk modulus is employed and the linear portion of dB/dT is selected for the calculation. For compounds exhibiting phase transitions, only the linear slope before the transition is used.In principle, an estimate of the Grüneisen parameter can be obtained from the temperature derivative of any elastic modulus, though the estimate will inevitably depend on the used modulus. This reflects the fact that (i) the elastic-tensor anisotropy can diverge with temperature (*i.e.*, C_{11} might soften faster than C_{44}, leading to a temperature dependent μ); (ii) moduli like Y and G can have significantly different magnitudes at low temperature, but still tend towards zero close to the melting (not the case for B), thus necessarily implying different temperature derivatives. As an example, Figure Sx (Supplemental Material) shows the variability in the estimated gamma for some relevant materials, employing different moduli in the Ledbetter equation. Although general material trends can be inferred, in some cases estimates from different moduli can differ more than the 250%. Consistency is therefore essential when comparing different materials.

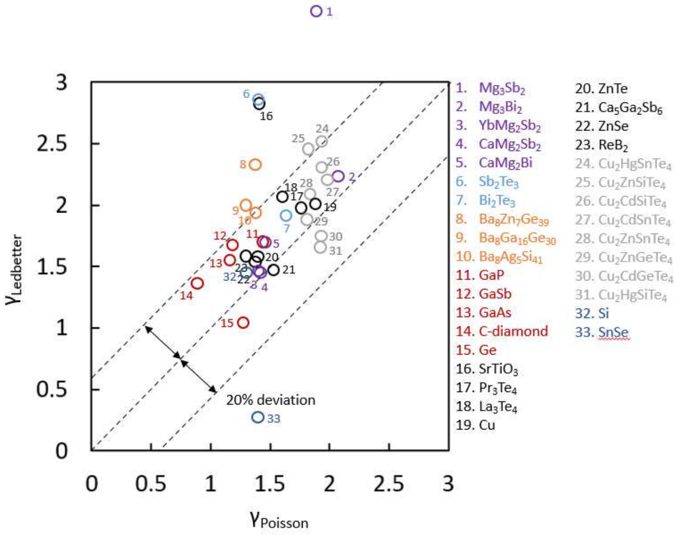

Fig. 10 A comparison of Grüneisen parameter estimates calculated from Eq. 2 and Eq. 11. Experimental Poisson's ratio and temperature-dependent Bulk modulus data were used[21,32,61,63,64,77,105–109]. The data can be find in Supplemental Table 2. The dashed lines indicate a 20% deviation from an ideal 1-to-1 agreement.

4.5.2 Poisson's ratio

Since experimental and computed room temperature elastic moduli are more widely available than temperature-dependent data, an expression relating γ to the Poisson's ratio, μ, has recently gained popularity[110–113]. Eq. 10 was initially derived within the

Debye model for a cubic system but has been shown to provide reasonable results for other symmetries as well[110].

$$\gamma = \frac{3}{2}\frac{B}{\rho\bar{v}^2} \tag{10}$$

Here, $\bar{v}$ is the root mean square velocity ($\bar{v}^2 = \frac{v_L^2+2v_T^2}{3}$). By considering that $\bar{v}^2 = \frac{C_{11}+2C_{44}}{3\rho}$ and $B = \frac{C_{11}+2C_{12}}{3}$, we can see that γ reduces to 1 when $C_{12} = C_{44}$. Therefore, the estimate of Grüneisen parameter from Eq. 10 can be practically interpreted as the difference between C_{12} and C_{44} ($i.e.(C_{11}+2C_{12})/(C_{11}+2C_{44})$), or in other words, how uniformly the material reacts to a given strain. By substituting the expressions for $\bar{v}$, B and μ one can obtain a single variable equation:

$$\gamma_{Poisson} = \frac{3}{2}\left(\frac{1+\mu}{2-3\mu}\right). \tag{11}$$

As $\gamma_{Poisson}$ increases monotonically as a function of μ in the range covered by most materials (μ = 0-0.5), a large μ can be considered a hallmark of a large Grüneisen parameter.

4.5.3 Thermal expansion

The most common method to estimate the Grüneisen parameter relies on thermal expansion. When the Einstein heat capacity and the quasi-harmonic approximation (*i.e.*, when ω is the only term that is affected by volume) are applied to Eq. 9 and combined with the Maxwell relations, Eq. 12 can be derived.

$$\gamma_\alpha = \frac{\alpha B}{C_V\rho} \tag{12}$$

Here, α is the volumetric thermal expansion. It is to be remembered that in the case of a material with large positive and negative mode Grüneisen parameters, the weighted average might be a small positive value, which would lead one to falsely conclude that the material is harmonic (thus possessing γ=0). Indeed, materials designed to have zero thermal expansion are not perfectly harmonic solids - rather, their structures allow for phonon modes with highly negative γ_i[114].

4.5.4 Discussion

Although the above calculation methods for the Grüneisen parameter are derived from the same origin, they are measuring fundamentally different phenomena, all of which are tied to anharmonicity. For this reason, they provide somewhat different estimates. This can be misleading when comparing materials if different expressions have been used. However, general conclusions can still be drawn. A comparison of $\gamma_{Poisson}$ (Eq. 11) and $\gamma_{Ledbetter}$ (Eq. 2) for a variety of materials is shown in Fig. 10. Figure 11a instead shows the functional trends of $\gamma_{Ledbetter}$ (here from dG/dT) and $\gamma_{Poisson}$ (alongside a comparison with the γ_α value), while Figure 11b compares the thermodynamic and DFT estimates for selected relevant compounds. All the data can be found in the Supplementary Table 2. The approximations show some agreement with respect to general trends. For example, diamond, Ge, and Si are found to be relatively harmonic (low γ), while Mg_3Sb_2 and Mg_3Bi_2 have overall more anharmonic bonding. However, there are also notable disparities among the methods. For example, since $\gamma_{Ledbetter}$ is calculated from a non-normalized temperature derivative of elastic moduli, it tends to be overemphasized for very hard materials, such as diamond. As such, comparing the anharmonicity of diamond and Ge, $\gamma_{Ledbetter}$ is higher for the former whereas $\gamma_{Poisson}$ is larger for Ge. Based on the functional forms and commonly adopted values of dG/dT and μ, $\gamma_{Ledbetter}$ can adopt a larger range of values than $\gamma_{Poisson}$, overall leading to more spread out and generally higher values for the former. This can indicate a greater sensitivity of the elastic moduli method in estimating the thermodynamic Grüneisen parameter.

In general, highly anharmonic materials have both high thermal expansion coefficients and a high rate of softening. However, elastic moduli soften at a faster rate than volume increases. For example, Mg_3Sb_2, among the most anharmonic TE materials, shows a 20% decrease in Y (as well as B and G) from room temperature to 300°C[63], while the volume increases of less than 1.5% in the same range[63]. On the other hand, a comparatively harmonic material like silicon exhibits more than one order of magnitude lower softening at high temperature (2% decrease in Y from room temperature to 300°C[124]), while around three times lower thermal expansion[116,125]. Negative thermal expansion materials present an interesting conundrum, as they can still exhibit pronounced softening with increasing temperature[126]. For such materials, one would obtain a negative Grüneisen parameter from Eq. 12. The Ledbetter formula is ambiguous in this regard, as we can choose the negative or positive root as solution of Eq. 2. Nevertheless, for this last one, regardless of the sign of γ, a material will soften with increasing temperature. Eq. 11, in contrast, only allows positive values of γ for physical values of Poisson's ratio.

Ultimately, even though the thermodynamic approximations of γ discussed here can reveal trends in materials, none can be regarded as a full replacement of in-depth computational or experimental characterizations.

5 Key recent results

In this section we illustrate some recent results highlighting different ways in which elastic moduli turned out valuable in studying thermoelectrics. Elastic moduli can provide important insights on the bonding chemistry, as well as on the thermal transport behavior, allowing to decouple contributions to κ_L due to the phonon group velocity, and phonon scattering and anharmonicity.

Furthermore, they represent a useful tool for an in-depth study of phase transitions. They are especially convenient when dealing with second-order ones. Indeed, in first-order phase transitions the first derivatives of the Gibbs energy G (and thus most material properties, e.g. density) are discontinuous at the transition. In contrast, second-order transitions involve continuous first derivatives of G and thus a gradual change of material properties[127–130,130–133]. For this reason, clear sings of discontinuities must be searched in physical properties connected with the second-order derivative. Second order derivatives of G include thermal expansion, specific heat, and elastic moduli[134]. While each of these parameters can be used to reveal a second order phase transition, it is worth noting that the specific heat is a scalar, and thermal expansion is a vector. Instead, the elastic moduli are

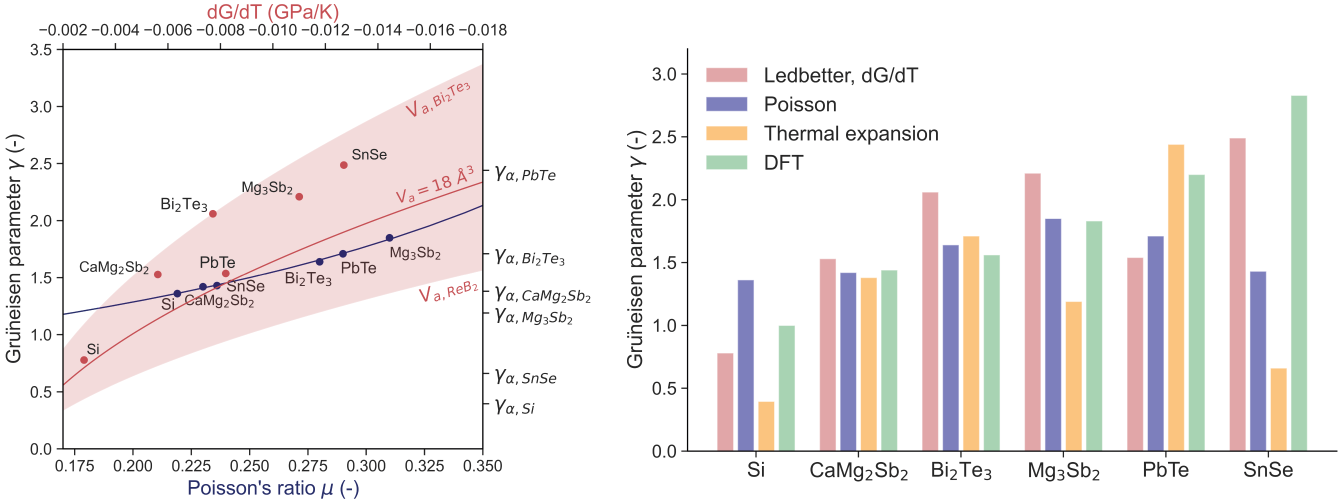

(a) (b)

Fig. 11 a) Functional forms of the Grüneisen parameters calculated from elastic moduli softening (Eq. 2) and Poisson's ratio (Eq. 11). As visible, the former gives a larger spreading of values thus possibly a greater sensitivity than the latter. Calculated γ for different materials are reported, alongside the estimation of γ from the thermal expansion (Eq. 12) for comparison. b) Bar plot comparing the different estimates of Grüneisen parameter for selected relevant materials. Data from refs. Si [115–117], $CaMg_2Sb_2$ and Mg_3Sb_2 [63], Bi_2Te_3 [64,118,119], PbTe [100,120,121], SnSe [71,122,123].

described by a fourth-order tensor, and thus carry the full symmetry of the discontinuities through a second-order transition. The effect of structural phase transitions on elastic constants has been studied extensively. Examples among functional materials include the ferroelectrics $BaTiO_3$, $SrTiO_3$ [135,136], $EuTi_{1-x}Nb_xO_3$ [137] and $Cd_2Re_2O_7$ [138], as well as several thermoelectric materials such as $Sn_xGe_{1-x}T$ [19,139–141], Zn_4Sb_3 [142], and Mg_2Si [143].

5.1 Case Study - Discovery of anharmonic inter-layer bonding in Mg_3Pn_2 (Pn=Sb,Bi)

AM_2X_2 compounds with the $CaAl_2Si_2$ ($P\bar{3}m1$) structure type (Figure 12a, where A is an alkali, alkaline earth, or rare earth metal, M is Mg, Al, or a transition metal, and X belongs to the IVA-VIA groups) have attracted interest in thermoelectrics because of their chemical diversity and tunability [144,145]. Mg_3Pn_2 have recently emerged as promising candidates of this class, also due to their exceptionally low κ_L. In fact, they exhibit values 2-3 times lower compared to isostructural $CaMg_2Pn_2$ and $YbMg_2Pn_2$ despite the larger, heavier cations in the latter compounds (Fig. 12f)) [144,146–148]. High temperature elastic moduli measurements, combined with high pressure XRD and *ab initio* phonon calculations were decisive in shedding light on this unusual thermal behaviour.

It was found that Mg_3Sb_2 and Mg_3Bi_2 possess exceptionally low elastic moduli (Fig. 6) with anomalously rapid softening rate (Fig. 12d), pointing to a high degree of anharmonicity. These properties are expected to have a major contribution to thermal transport and were found arising from the atomic arrangement. AM_2X_2 compounds can be described as covalently bonded $[A_2X_2]^{2-}$ tetrahedral slabs sandwiched between monolayers of A^{2+} cations (Fig. 12a) [144,149]. In Mg_3Pn_2, Mg occupies the octahedrally-coordinated A-site, defined as Mg(1) here, and the tetrahedrally-coordinated M-site, referred to as Mg(2). Both the Mg(1)-Pn and Mg(2)- Pn bonds have similar ionic character [150]. However, the different bond lengths (*i.e.* , 3.12 Å for Mg(1)-Sb and 2.88 Å for Mg(2)-Sb) and coordination environment lead to stiff tetrahedral Mg(2)-Pn and weak octahedral Mg(1)-Pn bonds. This has been confirmed by high-pressure XRD, showing a higher compressibility of the latter bond [151], as well as phonon calculations [63], pointing to a softer character for the Mg(1) over Mg(2) phonon modes.

The weak bonding between Mg(1) and Pn render the entire structure unstable with respect to inter-layer shear stress, as evidenced by the unusually low shear moduli [63]. This instability further leads to a high degree of anharmonicity, as confirmed by the large DFT Grüneisen parameter associated with these vibrational modes (see Fig. 12c), as well as the rapid softening observed in the experimental moduli with temperature (see Fig 12d). The anharmonicity associated to the Mg(1)-Pn bonds leads to enhanced phonon scattering and thus suppressed κ_L. One possible explanation for why only compounds with A = Mg (not those with A = Yb, Ca, Sr, Eu) exhibit anomalous thermal properties can be traced to the ionic radii. In the sphere packing model proposed by Pauling for ionic solids, the smallest stable cation to anion radius for an octahedral coordination is given by r_{cation}:r_{anion}=0.414. Fig. 12b) shows the estimated r_{cation}:r_{anion} for AMg_2Pn_2 solids, in which compounds with A = Mg have r_{cation}:r_{anion} below the stability limit, while those with larger cations are predicted to be stable in a six-fold coordinated environment. This can be the reason of the unstable inter-layer bonding leading to the anharmonic behaviour. For additional details, we refer the readers to refs. [63] and [151].

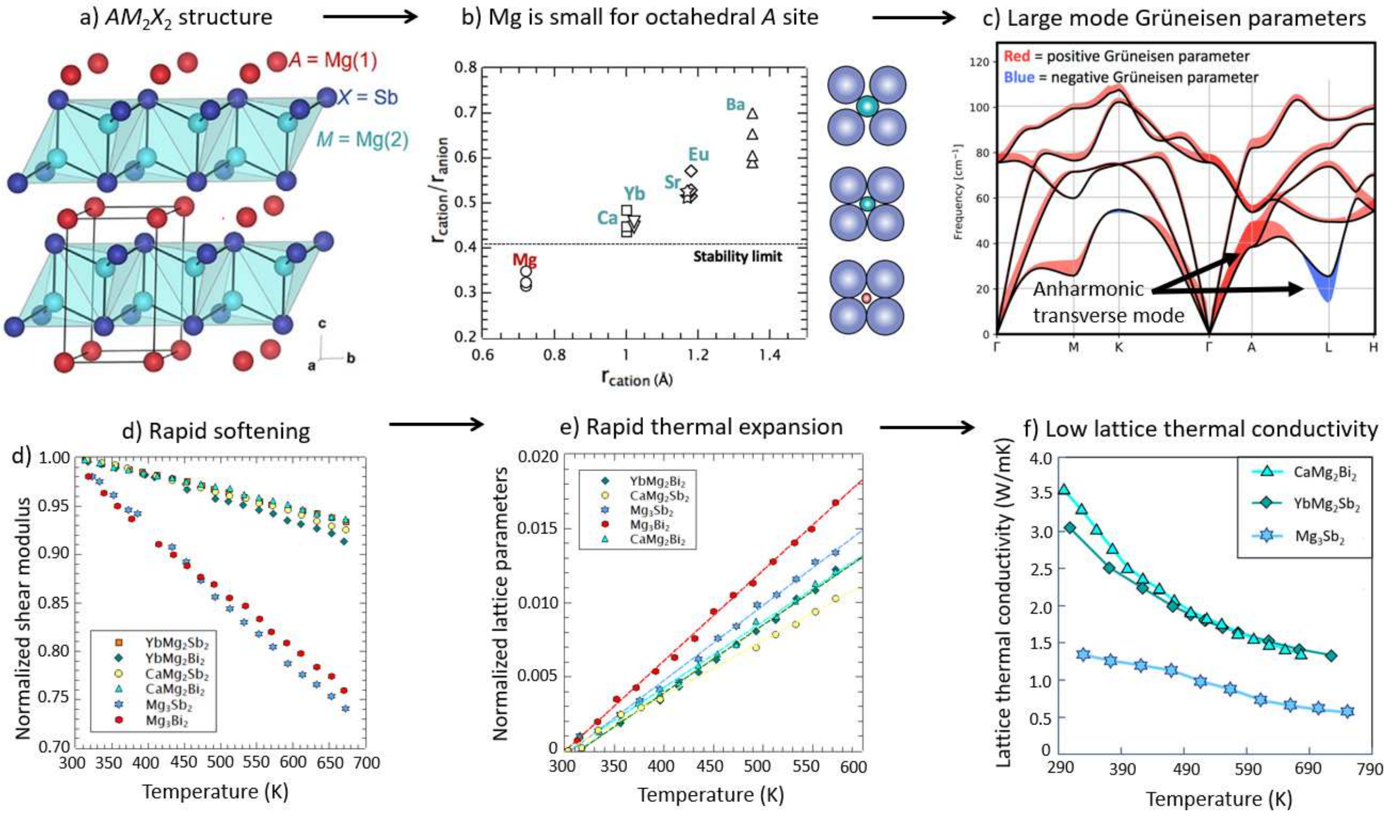

Fig. 12 a) The structure of AM_2X_2 compounds. b) When Mg occupies the octahedral A-site, the cation to anion size ratio falls below the stability limit according to Pauling's radius rule. c) The phonon dispersion of the Mg_3Sb_2 at low frequencies. Among AMg_2Pn_2 compounds, Mg_3Sb_2 and Mg_3Bi_2 have the fastest softening rate as shown by d) the normalized shear modulus, G/G_{300}, and e) they have the highest rate of thermal expansion. These features point to a high degree of anharmonicity. f) A comparison of the lattice thermal conductivity of AMg_2Sb_2 with A=Mg, Ca, and Yb[146–148], shows that Mg_3Sb_2 possesses the lowest values, in contradiction to typical trends between κ_L and mass.

5.2 Case Study - Quantifying scattering due to disorder in diamond like semiconductors

The quaternary tellurides Cu_2ABTe_4, where A = Zn, Hg, Cd, and B = Si, Sn, Ge, are a family of compounds possessing a diamond-like structure (DLS). They belong to the broader class of quaternary chalcogenides, which enormous chemical and structural freedom leads to highly tunable properties, with some compositions being suitable for photovoltaic (typically sulfides or selenides) and thermoelectric applications[152–154]. This class of materials is characterized by significant site disorder (anti-site defects) and the existence of order-disorder phase transitions affecting both thermal and electrical properties[155–157]. Quaternary DLS compounds exhibit different cation ordering motifs in close energetic proximity to one another (e.g., stannite and kesterite). For this reason, within a given structure type it is frequent to form anti-site defects. In the ideal, ordered stannite structure (Fig. 13a), the A and B cations are confined to specific layers. When both A and B are large atoms (e.g., Sn and Hg), strain is developed in the a direction. As temperature increases, the structure can relieve this strain by becoming increasingly disordered, with the large atoms diffusing into the Cu-containing layers (Fig. 13a).

High temperature measurements of elastic moduli helped understanding the connection between site disorder and the observed ultra-low κ_L in certain DLS compounds, as well as proved effective in detecting the critical temperature of the disordering phenomena. Indeed, order-disorder transitions in DLS compounds are generally second-order, meaning that the variation of lattice parameters with temperature is continuous (no sharp discontinuity). In contrast, the elastic moduli can change abruptly, revealing the transition temperature, T_c. In a study of a series of Cu_2ABTe_4 compounds by Ortiz el.al[21], a change in slope of the temperature-dependent elastic moduli and sound velocities was detected with RUS (Fig. 13b) and correlated with an order-disorder phase transition. Interestingly, above T_c all the compounds exhibit an increase in softening rate (larger negative slope), mostly corresponding to a further suppression in κ_L.

As can be seen in Fig. 13b), the Cu_2ABTe_4 compounds display relatively small variations in the magnitude of sound velocity (no more than 20% difference). Nevertheless, the room temperature κ_L of Hg-containing quaternary compounds is more than three times lower than that of Zn-containing ones (e.g., κ_L = 3.8 W/mK and 1.1 W/mK for $Cu_2ZnGeTe_4$ and $Cu_2HgSnTe_4$, respectively). By combining the measured κ_L and v_{sound}, an estimate of the mean phonon relaxation time τ as a function of temperature was extracted using Eq. 3. A drastic decrease in τ for the Hg-containing samples was found and hypothesized connected with a change in point defect scattering. To quantify the impact of different types of anti-site defects, the authors investigated the overlap integrals of the partial density of states (PDOS) of individual atoms, revealing a trend between the PDOS overlap and κ_L. They found that anti-site defects comprised of atoms with dissimilar PDOS (exemplified by Cu and Hg) perturb the associated phonon modes more strongly than defects with nearly identical PDOS, thus explaining the contrast in τ among DLS compounds and the remarkably low κ_L in Hg-based ones. For additional details, we refer the readers to ref.[21].

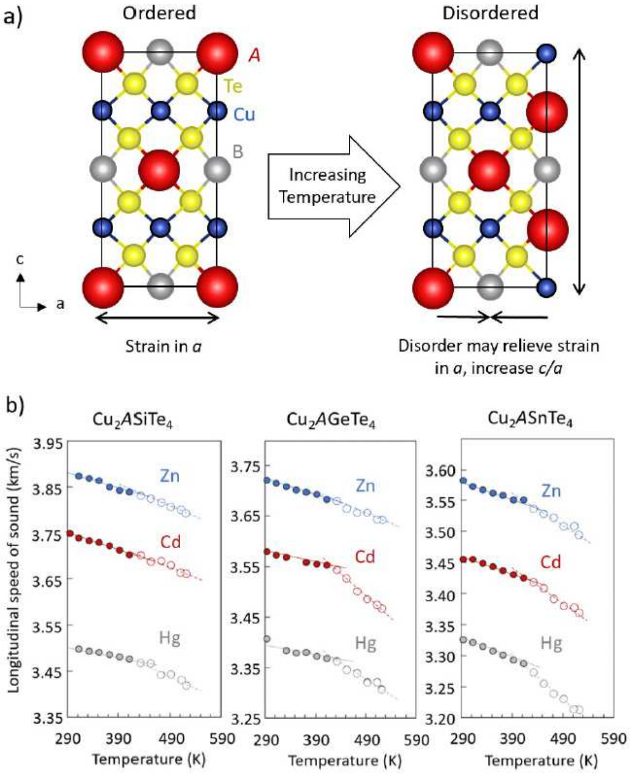

Fig. 13 a) A schematic representation of the order-disorder phase transition for Cu_2ABTe_4 compounds (A = Zn, Cd, Hg, and B = Si, Ge, Sn). b) The elastic moduli of DLS Cu_2ABTe_4 with A = Zn, Hg, Cd, and B = Si, Sn, Ge[21]. At around 430 K, discontinuities in the temperature-dependent speed of sound measured by RUS can be observed for all nine compounds.

5.3 Case Study - Mapping the transition from a 2D to a 3D structure in $(GeTe)_{17}Sb_2Te_3$

(GeTe)-(Sb_2Te_3) alloys (abbreviated as GST) have been studied extensively as materials for phase-change random-access memory applications[158–160]. In recent years, Ge-rich GST has also attracted attention in thermoelectrics for the excellent performance ($zT>2$) and reduced thermal conductivity compared to pure GeTe[161–164]. Similarly to GeTe[165], GST alloys exhibit a reversible transition from an ambient temperature rhombohedral to a high temperature rock-salt cubic structure[64,166,167]. However, the incorporation of Sb_2Te_3 leads to van der Waals gaps causing fascinating elastic properties, as described below. In the high-temperature rock-salt structure, the cation sublattice is randomly occupied by Ge, Sb, and vacancies, while Te occupies the anion sublattice. In contrast, the rhombohedral structure contains covalent, fully occupied slabs, which are interrupted by ordered layers of cation vacancies. These vacancy layers can be effectively described as van der Waals gaps (Fig. 14a) and confer a two-dimensional structure to the material. Unlike pure GeTe, in which the rhombohedral to cubic transition is rapid and involves only a local displacement of the cation positions[20], the phase transition in GST alloys necessitates of a dynamic reconfiguration of the vacancies. Cations must diffuse from the covalent slabs to fill the vacancy layers. Concurrently, vacancies get randomly dispersed into the matrix.

Peng et al. investigated the impact of the phase transition on the thermal expansion and elastic moduli of polycrystalline $Ge_{17}Sb_2Te_{20}$. The study allowed to identify the role of vacancy diffusion on the anomalous lattice thermal conductivity, which featured a mostly flat trend with a sharp increase at the transition.[64] Fig. 14b) shows the Young's modulus normalized to 300 K (Y/Y_0) of $Ge_{17}Sb_2Te_{20}$ compared with Sb_2Te_3 and GeTe. Although all three compounds were shown to have similar rates of volumetric thermal expansion, they exhibit drastic differences in the temperature-dependence of the elastic moduli. $Ge_{17}Sb_2Te_{20}$, while in the rhombohedral structure, shows unique elastic moduli stiffening with temperature. This behaviour contrasts with pure Sb_2Te_3 and GeTe, both of which exhibit the usual softening with increasing temperature. The stiffening of rhombohedral $Ge_{17}Sb_2Te_{20}$ with temperature likely compensates the expected increase in phonon-phonon scattering thus explaining the flat trend of κ_L. This stiffening was attributed to (i) the gradual decrease in the rhombohedral distortion with temperature, (ii) the progressive diffusion of cation vacancies from the van der Waals layers into the surrounding slabs. This suggests that a crystal structure with randomly distributed vacancies is stiffer than one with ordered vacancy layers. Consistently, at the phase transition to the cubic symmetry, $Ge_{17}Sb_2Te_{20}$ shows an abrupt increase in Young's modulus. This is in accordance with the reported behaviour of GeTe-SnTe alloys through an analogous rhombohedral to cubic transition[139]. Softening of the elastic moduli can instead be observed above the phase transition, as expected due to thermal expansion.

Through a combination of structural and elasticity measurements, the study maps the progressive vacancy diffusion in $Ge_{17}Sb_2Te_{20}$ leading to an anomalous lattice hardening. This progressive structural stiffening explains the flat temperature dependence of κ_L as well as the step observed with the transition to the fully 3D cubic structure. For additional details, we refer the readers to ref.[64].

6 Summary and outlook

Our aim with the present review is to emphasize the importance and utility of experimental elasticity measurements, especially at high-temperature, in improving our understanding of underlying relationships between chemical bonding and transport physics. A survey of the existing literature on temperature-dependent elastic moduli of thermoelectric materials is used to highlight the relationship between bonding and properties that control thermal conductivity. In particular, we see that differences in bond stiff-

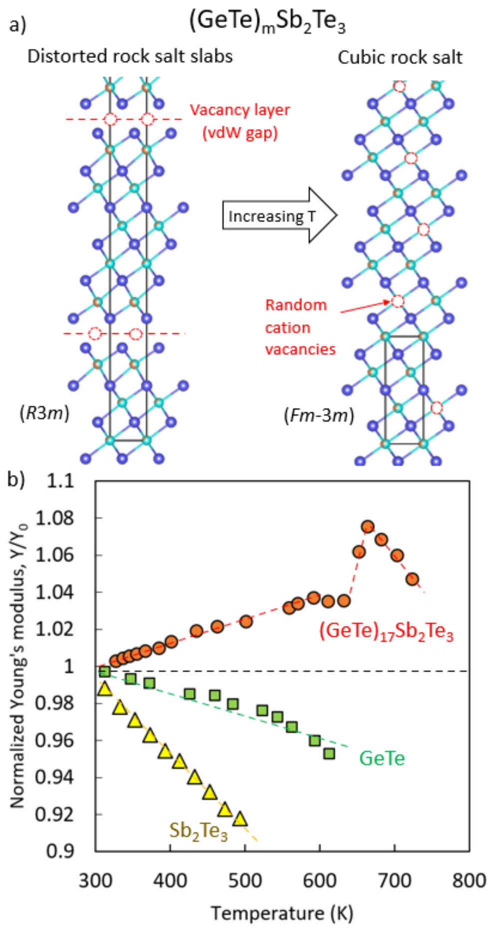

Fig. 14 a) The structure of $(GeTe)_{17}Sb_2Te_3$ before and after the phase transition. b) Temperature versus the Young's modulus normalized to 300 K of $(GeTe)_{17}Sb_2Te_3$, Sb_2Te_3, and GeTe. $(GeTe)_{17}Sb_2Te_3$ stiffens with increasing temperature.

,

ness lead to wide variations in the acoustic speed of sound and Grüneisen parameter. We also present case-studies to show the remarkable sensitivity of temperature-dependent elasticity measurements in interpreting thermal conductivity trends, as well as detecting phase transitions.

As valuable as elasticity data is for understanding properties, the elastic moduli and their relationship with lattice thermal conductivity remains unexplored for the vast majority of thermoelectric materials. While it has become increasingly common to see reports of room-temperature speed of sound, these results are too often presented in a cursory fashion. Significant value could be gleaned via accurate analyses of elastic moduli data, especially if compared with related materials, allowing to determine whether changes in the speed of sound (and hence thermal conductivity) are due to differences in chemical bonding or other effects, like microstructure.

While the present review emphasized stand-alone measurements of elastic moduli, in particular via acoustic techniques, a further prolific opportunity is combining them with other in-situ techniques. For example, by coupling elasticity measurements with Raman spectroscopy and inelastic neutron or X-ray scattering, one can gain a complete and detailed picture of the phonon spectrum of a material. The elastic moduli provide accurate information about low energy acoustic phonons, while Raman spectroscopy yields the frequencies of selected optical modes, and inelastic scattering can be used to target any desired phonon mode.In each technique, temperature-dependent measurements can be used to provide an estimate of the anharmonicity (Grüneisen parameter) of various phonons. *Ab initio* phonon calculations are becoming increasingly powerful as well, and now include open-source visualization tools that can help chemists draw direct connections between specific chemical bonds and the associated vibrational modes. Combining them with experimental measurements of elastic moduli, carefully analysed with the methods described above, can help constructing a comprehensive understanding of the thermal conductivity in solids.

Conflicts of Interest

There are no conflicts of interest to declare.

Acknowledgements

This work is supported by the U.S. Department of Energy (DOE), Office of Basic Energy Sciences, Division of Materials Sciences and Engineering under Award No. DE-SC0019252.

Notes and references

1 F. J. DiSalvo, *Science*, 1999, **285**, 703–706.
2 D. R. Askeland, P. P. Phulé, W. J. Wright and D. Bhattacharya, *The science and engineering of materials*, Springer, 2003.
3 M. E. Gurtin, *Linear theories of elasticity and thermoelasticity*, Springer, 1973, pp. 1–295.
4 F. J. Freibert, J. N. Mitchell, T. A. Saleh and A. Migliori, *Instability and Anharmonicity in Plutonium Thermo-physical Properties*, 2012.
5 B. Vodar and P. Marteau, *High pressure science and technology. Proceedings of the VIIth international AIRAPT Conference. Part_I, II. Conference held at Le Creusot, France, 30 July-3 August 1979.*, 1980.
6 E. Cowley, Z. Gong and G. Horton, *Physical Review B*, 1990, **41**, 2150.
7 R. G. Leisure and F. Willis, *Journal of Physics: Condensed Matter*, 1997, **9**, 6001.
8 F. Guinea and C. Tejedor, *Journal of Physics C: Solid State Physics*, 1982, **15**, 755.
9 A. R. Murphy, F. Murphy-Armando, S. Fahy and I. Savić, *Physical Review B*, 2018, **98**, 085201.
10 B. Nag and S. Gangopadhyay, *Semiconductor science and technology*, 1995, **10**, 813.
11 A. Migliori, *Resonant ultrasound spectroscopy*, 2016.
12 Y. K. Lee, K. Ahn, J. Cha, C. Zhou, H. S. Kim, G. Choi, S. I. Chae, J.-H. Park, S.-P. Cho, S. H. Park *et al.*, *Journal of the American Chemical Society*, 2017, **139**, 10887–10896.
13 U. Aseginolaza, R. Bianco, L. Monacelli, L. Paulatto, M. Calandra, F. Mauri, A. Bergara and I. Errea, *Physical review letters*, 2019, **122**, 075901.

14 M. Sist, J. Zhang and B. Brummerstedt Iversen, *Acta Crystallographica Section B: Structural Science, Crystal Engineering and Materials*, 2016, **72**, 310–316.
15 X. X. Xiao, J. X. Xie, T. X. Feng and J. Z. Q., *Chinese Physics B*, 2011, **20**, 087201.
16 S. Ballikaya, H. Chi, J. R. Salvador and C. Uher, *Journal of Materials Chemistry A*, 2013, **1**, 12478–12484.
17 Z. Liu, J. Sun, J. Mao, H. Zhu, W. Ren, J. Zhou, Z. Wang, D. J. Singh, J. Sui, C.-W. Chu *et al.*, *Proceedings of the National Academy of Sciences*, 2018, **115**, 5332–5337.
18 Y. Qiu, Y. Jin, D. Wang, M. Guan, W. He, S. Peng, R. Liu, X. Gao and L.-D. Zhao, *Journal of Materials Chemistry A*, 2019, **7**, 26393–26401.
19 U. D. Wdowik, K. Parlinski, S. Rols and T. Chatterji, *Physical Review B*, 2014, **89**, 224306.
20 T. Chatterji, C. Kumar and U. D. Wdowik, *Physical Review B*, 2015, **91**, 054110.
21 B. R. Ortiz, W. Peng, L. C. Gomes, P. Gorai, T. Zhu, D. M. Smiadak, G. J. Snyder, V. Stevanovic, E. Ertekin, A. Zevalkink *et al.*, *Chemistry of Materials*, 2018, **30**, 3395–3409.
22 S. Chen, A. Walsh, Y. Luo, J.-H. Yang, X. Gong and S.-H. Wei, *Physical Review B*, 2010, **82**, 195203.
23 X. Fontané, V. Izquierdo-Roca, E. Saucedo, S. Schorr, V. Yukhymchuk, M. Y. Valakh, A. Pérez-Rodríguez and J. Morante, *Journal of Alloys and Compounds*, 2012, **539**, 190–194.
24 S. Schorr, H.-J. Hoebler and M. Tovar, *European Journal of Mineralogy*, 2007, **19**, 65–73.
25 R. McKinney, P. Gorai, E. S. Toberer and V. Stevanovic, *Chemistry of Materials*, 2019, **31**, 2048–2057.
26 P. Gorai, R. W. McKinney, N. M. Haegel, A. Zakutayev and V. Stevanovic, *Energy & Environmental Science*, 2019, **12**, 3338–3347.
27 P. Gorai, A. Goyal, E. S. Toberer and V. Stevanović, *Journal of Materials Chemistry A*, 2019, **7**, 19385–19395.
28 M. De Jong, W. Chen, T. Angsten, A. Jain, R. Notestine, A. Gamst, M. Sluiter, C. K. Ande, S. Van Der Zwaag, J. J. Plata *et al.*, *Sci. Data*, 2015, **2**, 150009.
29 R. E. Newnham, *Properties of materials: anisotropy, symmetry, structure*, Oxford University Press on Demand, 2005.
30 J. F. Nye, *Physical Properties of Crystals*, 2006.
31 *The Materials Project*, `https://materialsproject.org/`, Accessed: 2022-07-16.
32 Y. Suzuki, J. B. Levine, A. Migliori, J. D. Garrett, R. B. Kaner, V. R. Fanelli and J. B. Betts, *The Journal of the Acoustical Society of America*, 2010, **127**, 2797–2801.
33 M. De Jong, W. Chen, T. Angsten, A. Jain, R. Notestine, A. Gamst, M. Sluiter, C. K. Ande, S. Van Der Zwaag, J. J. Plata, C. Toher, S. Curtarolo, G. Ceder, K. A. Persson and M. Asta, *Scientific Data*, 2015, **2**, 1–13.
34 J. O. Jenkins, J. A. Rayne and R. W. Ure, *Physical Review B*, 1972, **5**, 3171–3184.
35 W. G. Zeier, A. Zevalkink, Z. M. Gibbs, G. Hautier, M. G. Kanatzidis and G. J. Snyder, *Angewandte Chemie International Edition*, 2016, **55**, 6826–6841.
36 C. A. Klein and G. F. Cardinale, *Diamond and Related Materials*, 1993, **2**, 918–923.
37 F. Greco, A. Zucca, S. Taccola, A. Menciassi, T. Fujie, H. Haniuda, S. Takeoka, P. Dario and V. Mattoli, *Soft Matter*, 2011, **7**, 10642–10650.
38 R. Hanus, M. T. Agne, A. J. Rettie, Z. Chen, G. Tan, D. Y. Chung, M. G. Kanatzidis, Y. Pei, P. W. Voorhees and G. J. Snyder, *Advanced Materials*, 2019, **31**, year.
39 J. P. Male, R. Hanus, G. J. Snyder and R. P. Hermann, *Chemistry of Materials*, 2021, **33**, 4765–4772.
40 T. hang and J. E. Hack, *Physica Status Solidi (a)*, 1992, **131**, 437–443.
41 M. Grewer, J. Markmann, R. Karos, W. Arnold and R. Birringer, *Acta Materialia*, 2011, **59**, 1523–1529.
42 *In preparation*, 2020.
43 W. Overton Jr and J. Gaffney, *Physical Review*, 1955, **98**, 969.
44 Y. Varshni, *Physical Review B*, 1970, **2**, 3952.
45 H. Ledbetter, M. Lei, A. Hermann and Z. Sheng, *Physica C: Superconductivity*, 1994, **225**, 397–403.
46 H. McSkimin, *Physical Acoustics*, 1964, **1**, 271–334.
47 Y. Eckstein, A. W. Lawson and D. H. Reneker, *Journal of Applied Physics*, 1960, **31**, 1534–1538.
48 G. Li and J. Gladden, *International Journal of Spectroscopy*, 2010.
49 B. J. Zadler, J. H. Le Rousseau, J. A. Scales and M. L. Smith, *Geophysical Journal International*, 2004, **156**, 154–169.
50 J. Torres, A. Flores-Betancourt and R. P. Hermann, *The Journal of the Acoustical Society of America*, 2022, **151**, 3547–3563.
51 H. H. Demarest Jr, *The Journal of the Acoustical Society of America*, 1971, **49**, 768–775.
52 Y. SUMINO, O. NISHIZAWA, T. GOTO, I. OHNO and M. OZIMA, *Journal of Physics of the Earth*, 1977, **25**, 377–392.
53 C. S. Mejía, A. K. Nayak, J. A. Schiemer, C. Felser, M. Nicklas and M. A. Carpenter, *Journal of Physics: Condensed Matter*, 2015, **27**, 415402.
54 J. A. Bell, W. R. Bennett, R. Zanoni, G. I. Stegeman, C. M. Falco and F. Nizzoli, *Phys. Rev. B*, 1987, **35**, 4127–4130.
55 A. Polian, M. Grimsditch and I. Grzegory, *Journal of Applied Physics*, 1996, **79**, 3343–3344.
56 M. Grimsditch, E. S. Zouboulis and A. Polian, *Journal of Applied Physics*, 1994, **76**, 832–834.
57 R. H. Marion and J. B. Cohen, *Advances in X-ray Analysis*, 1976, **20**, 355–367.
58 A. K. Singh, H.-k. Mao, J. Shu and R. J. Hemley, *Phys. Rev. Lett.*, 1998, **80**, 2157–2160.
59 C. J. Howard and E. H. Kisi, *Journal of Applied Crystallography*, 1999, **32**, 624–633.
60 W. Zhou, H. Wu and T. Yildirim, *Phys. Rev. B*, 2007, **76**, 184113.
61 N. L. Okamoto, T. Nakano, K. Tanaka and H. Inui, *Journal of Applied Physics*, 2008, **104**, 013529.

62 G. Rogl, A. Grytsiv, M. Gürth, A. Tavassoli, C. Ebner, A. Wünschek, S. Puchegger, V. Soprunyuk, W. Schranz, E. Bauer *et al.*, *Acta Materialia*, 2016, **107**, 178–195.

63 W. Peng, G. Petretto, G.-M. Rignanese, G. Hautier and A. Zevalkink, *Joule*, 2018, **2**, 1879–1893.

64 W. Peng, D. M. Smiadak, M. G. Boehlert, S. Mather, J. B. Williams, D. T. Morelli and A. Zevalkink, *Journal of Applied Physics*, 2019, **126**, 055106.

65 F. Ren, E. D. Case, J. R. Sootsman, M. G. Kanatzidis, H. Kong, C. Uher, E. Lara-Curzio and R. M. Trejo, *Acta Materialia*, 2008, **56**, 5954–5963.

66 R. D. Schmidt, E. D. Case, J. E. Ni, R. M. Trejo, E. Lara-Curzio, R. J. Korkosz, Kanatzidis and G. Mercouri, *J. mater. sci.*, 2013, **48**, 8244–8258.

67 R. Schwarz and J. Vuorinen, *Journal of Alloys and Compounds*, 2000, **310**, 243–250.

68 U. Lang, N. Naujoks and J. Dual, *Synthetic Metals*, 2009, **159**, 473–479.

69 B. Lu, H. Yuk, S. Lin, N. Jian, K. Qu, J. Xu and X. Zhao, *Nature communications*, 2019, **10**, 1–10.

70 A. Zevalkink, D. M. Smiadak, J. L. Blackburn, A. J. Ferguson, M. L. Chabinyc, O. Delaire, J. Wang, K. Kovnir, J. Martin, L. T. Schelhas *et al.*, *Applied Physics Reviews*, 2018, **5**, 021303.

71 A. Karunarathne, P. Parajuli, G. Priyadarshan, S. Bhattacharya, R. Rao, P. C. Wei, Y. Y. Chen, J. R. Gladden and A. M. Rao, *Physical Review B*, 2021, **103**, 54108.

72 L. D. Zhao, S. H. Lo, Y. Zhang, H. Sun, G. Tan, C. Uher, C. Wolverton, V. P. Dravid and M. G. Kanatzidis, *Nature*, 2014, **508**, 373–377.

73 G. P. M. C. Uher, J. Yang, S. Hu, D. T. Morelli, *International Conference on Thermoelectrics, ICT, Proceedings*, 1999, **59**, 531–534.

74 T. Park, C. Park, B. Kim, H. Shin and E. Kim, *Energy & Environmental Science*, 2013, **6**, 788–792.

75 R. W. Cahn, *Advanced Materials*, 1991, **3**, 628–629.

76 B. Lee and D. Lee, *CALPHAD: Comput. Coupling Phase Diagrams Thermochem*, 1992.

77 D. Cheikh, K. Lee, W. Peng, A. Zevalkink, J.-P. Fleurial and S. K. Bux, *Materials*, 2019, **12**, 734.

78 T. M. Tritt, *Thermal conductivity: theory, properties, and applications*, Springer Science & Business Media, 2005.

79 Z. Tian, J. Garg, K. Esfarjani, T. Shiga, J. Shiomi and G. Chen, *Physical Review B*, 2012, **85**, 184303.

80 S. Mukhopadhyay, L. Lindsay and D. J. Singh, *Scientific reports*, 2016, **6**, 37076.

81 T. Feng, L. Lindsay and X. Ruan, *Physical Review B*, 2017, **96**, 161201.

82 Y. Wang, Y. Sui, X. Wang, W. Su, X. Liu and H. J. Fan, *Acta materialia*, 2010, **58**, 6306–6316.

83 R. Berman and P. G. Klemens, *Physics Today*, 1978, **31**, 56.

84 E. S. Toberer, A. Zevalkink and G. J. Snyder, *J. Mater. Chem.*, 2011, **21**, 15843–15852.

85 S. F. Wang, Y. F. Hsu, J. C. Pu, J. C. Sung and L. G. Hwa, *Materials Chemistry and Physics*, 2004, **85**, 432–437.

86 J. Liu, X. Wang, D. Li, N. E. Coates, R. A. Segalman and D. G. Cahill, *Macromolecules*, 2015, **48**, 585–591.

87 J. E. Graebner, *Diamond: Electronic Properties and Applications*, 1995, 285–318.

88 Y. Gelbstein, *Journal of electronic materials*, 2011, **40**, 533–536.

89 G. Grimvall, *Thermophysical Properties of Materials*, 1999.

90 N. G. Pace and G. A. Saunders, *Journal of Physics and Chemistry of Solids*, 1971, **32**, 1585–1601.

91 J. Feng, B. Xiao, J. Chen, Y. Du, J. Yu and R. Zhou, *Materials & Design*, 2011, **32**, 3231–3239.

92 J. W. Jaeken and S. Cottenier, *Computer Physics Communications*, 2016, **207**, 445–451.

93 R. Mckinney, P. Gorai, E. S. Toberer and V. Stevanovic, *Chemistry of Materials*, 2019, **31**, 2048–2057.

94 Y. C. Akgoz, G. A. Saunders and Z. Sumengen, *Journal of Materials Science*, 1972, **7**, 279–288.

95 J. O. Jenkins, J. A. Rayne and R. W. Ure, *Physics Letters A*, 1969, **30**, 349–350.

96 J. Callaway, *Physical Review*, 1959, **113**, 1046–1051.

97 D. G. Cahill, S. K. Watson and R. O. Pohl, *Physical Review B*, 1992, **46**, 6131–6140.

98 J. Yan, P. Gorai, B. Ortiz, S. Miller, S. A. Barnett, T. Mason, V. Stevanović and E. S. Toberer, *Energy and Environmental Science*, 2015, **8**, 983–994.

99 S. A. Miller, P. Gorai, B. R. Ortiz, A. Goyal, D. Gao, S. A. Barnett, T. O. Mason, G. J. Snyder, Q. Lv, V. Stevanović and E. S. Toberer, *Chemistry of Materials*, 2017, **29**, 2494–2501.

100 F. Ren, E. D. Case, J. R. Sootsman, M. G. Kanatzidis, H. Kong, C. Uher, E. Lara-Curzio and R. M. Trejo, *Acta Materialia*, 2008, **56**, 5954–5963.

101 A. S. Pashinkin, M. S. Mikhailova, A. S. Malkova and V. A. Fedorov, *Inorganic Materials*, 2009, **45**, 1226–1229.

102 E. Grüneisen, *Annalen der Physik*, 1912, **39**, 257–306.

103 C. Li, O. Hellman, J. Ma, A. May, H. Cao, X. Chen, A. Christianson, G. Ehlers, D. Singh, B. Sales *et al.*, *Physical Review Letters*, 2014, **112**, 175501.

104 P. Verma, S. Abbi and K. Jain, *Physical Review B*, 1995, **51**, 16660.

105 B. Lee, *Journal of Applied Physics*, 1970, **41**, 2984–2987.

106 D. Su, Y.-L. He, J.-Q. Liu and X.-G. Lu, First International Conference on Information Sciences, Machinery, Materials and Energy, 2015.

107 S. Nikanorov and B. K. Kardashev, *MoIzN*, 1985.

108 W. Boyle and R. Sladek, *Physical Review B*, 1975, **11**, 2933.

109 Y. Burenkov, *Soviet Physics-Solid State*, 1973, **15**, 1175–1177.

110 D. Sanditov and M. Darmaev, *Inorganic Materials*, 2019, **55**, 617–622.

111 D. Sanditov and V. Belomestnykh, *Technical Physics*, 2011, **56**, 1619–1623.

112 V. N. Belomestnykh and E. P. Tesleva, *Technical physics*,

2004, **49**,.

113 V. N. Belomestnykh, *Technical Physics Letters*, 2004, **30**, 91–93.

114 D. Chang, W. Yu, Q. Sun and Y. Jia, *Physical Chemistry Chemical Physics*, 2017, **19**, 2067–2072.

115 H. J. McSkimin, *Journal of Applied Physics*, 1953, **24**, 988–997.

116 Y. Okada and Y. Tokumaru, *Journal of Applied Physics*, 1984, **56**, 314–320.

117 D. Cuffari and A. Bongiorno, *Physical Review Letters*, 2020, **124**, 215501.

118 L. M. Pavlova, Y. I. Shtern and R. E. Mironov, *High Temperature*, 2011, **49**, 369–379.

119 A. F. Zurhelle, V. L. Deringer, R. P. Stoffel and R. Dronskowski, *Journal of Physics Condensed Matter*, 2016, **28**, year.

120 M. T. Agne, *PhD thesis*, 2020, **21**, 1–9.

121 X. K. Wang, I. Veremchuk, M. Bobnar, J. T. Zhao and Y. Grin, *Inorganic Chemistry Frontiers*, 2016, **3**, 1152–1159.

122 Y. Xiao, C. Chang, Y. Pei, D. Wu, K. Peng, X. Zhou, S. Gong, J. He, Y. Zhang, Z. Zeng and L. D. Zhao, *Physical Review B*, 2016, **94**, 5–10.

123 D. Bansal, J. Hong, C. W. Li, A. F. May, W. Porter, M. Y. Hu, D. L. Abernathy and O. Delaire, *Physical Review B*, 2016, **94**, 32–42.

124 J. Vanhellemont, A. K. Swarnakar and O. Van der Biest, *ECS Transactions*, 2014, **64**, 283–292.

125 W. M. Yim and R. J. Paff, *Journal of Applied Physics*, 1974, **45**, 1456–1457.

126 F. R. Drymiotis, H. Ledbetter, J. B. Betts, T. Kimura, J. C. Lashley, A. Migliori, A. Ramirez, G. Kowach and J. Van Duijn, *Physical Review Letters*, 2004, **93**, 1–4.

127 E. K. H. Salje, *Acta Crystallographica Section A*, 1991, **47**, 453–469.

128 F. Gascoin and A. Maignan, *Chemistry of Materials*, 2011, **23**, 2510–2513.

129 M. Kirkham, P. Majsztrik, E. Skoug, D. Morelli, H. Wang, W. D. Porter, E. A. Payzant and E. Lara-Curzio, *Journal of Materials Research*, 2011, **26**, 2001–2005.

130 P. W. Anderson, *Basic Notions Of Condensed Matter Physics*, 2018.

131 L. Li, K. Nishimura, W. D. Hutchison, Z. Qian, D. Huo and T. NamiKi, *Applied Physics Letters*, 2012, **100**, 152403.

132 R. Hott, R. Kleiner, T. Wolf and G. Zwicknagl, *Digital Encyclopedia of Applied Physics*, 2016, 1–55.

133 M. Sigrist and K. Ueda, *Rev. Mod. Phys.*, 1991, **63**, 239–311.

134 P. Papon, J. Leblond and P. H. E. Meijer, *The Physics of Phase Transitions*, Springer-Verlag Berlin Heidelberg, 2006.

135 B. Lüthi and W. Rehwald, *Topics in Current Physics*, 1981, 131–184.

136 W. Rehwald, *Advances in Physics*, 1973, **22**, 721–755.

137 L. Li, J. R. Morris, M. R. Koehler, Z. Dun, H. Zhou, J. Yan, D. Mandrus and V. Keppens, *Phys. Rev. B*, 2015, **92**, 024109.

138 I. A. Sergienko, V. Keppens, M. McGuire, R. Jin, J. He, S. H. Curnoe, B. C. Sales, P. Blaha, D. J. Singh, K. Schwarz and D. Mandrus, *Phys. Rev. Lett.*, 2004, **92**, 065501.

139 T. Seddon, J. Farley and G. Saunders, *Solid State Communications*, 1975, **17**, 55–57.

140 D. Yang, T. Chatterji, J. A. Schiemer and M. A. Carpenter, *Phys. Rev. B*, 2016, **93**, 144109.

141 W. Rehwald and G. K. Lang, *Journal of Physics C: Solid State Physics*, 1975, **8**, 3287–3296.

142 S. Bhattacharya, R. P. Hermann, V. Keppens, T. M. Tritt and G. J. Snyder, *Phys. Rev. B*, 2006, **74**, 134108.

143 B. H. Yu and D. Chen, *Chinese Physics B*, 2011, **20**, 030508.

144 W. Peng, S. Chanakian and A. Zevalkink, *Inorg. Chem. Front.*, 2018, **5**, 1744–1759.

145 J. Zhang, L. Song and B. B. Iversen, *Npj Computational Materials*, 2019, **5**, 76.

146 J. Shuai, Y. Wang, H. S. Kim, Z. Liu, J. Sun, S. Chen, J. Sui and Z. Ren, *Acta Materialia*, 2015, **93**, 187–193.

147 A. F. May, M. A. McGuire, D. J. Singh, J. Ma, O. Delaire, A. Huq, W. Cai and H. Wang, *Physical Review B*, 2012, **85**, 035202.

148 A. Bhardwaj, A. Rajput, A. Shukla, J. Pulikkotil, A. Srivastava, A. Dhar, G. Gupta, S. Auluck, D. Misra and R. Budhani, *RSC advances*, 2013, **3**, 8504–8516.

149 J. Burdett and G. Miller, *Chem. Mater.*, 1990, **2**, 12–26.

150 J. Zhang, L. Song, M. Sist, K. Tolborg and B. B. Iversen, *Nature communications*, 2018, **9**, 1–10.

151 M. Calderón-Cueva, W. Peng, S. M. Clarke, J. Ding, B. L. Brugman, G. Levental, A. Balodhi, M. Rylko, O. Delaire, J. P. Walsh, S. M. Dorfman and A. Zevalkink, *Chemistry of Materials*, 2021, **33**, 567–573.

152 S. Chen, X. G. Gong, A. Walsh and S.-H. Wei, *Applied Physics Letters*, 2010, **96**, 021902.

153 S. R. Hall, J. T. Szymanski and J. M. Stewart, *The Canadian Mineralogist*, 1978, **16**, 131–137.

154 B. G. Mendis, M. D. Shannon, M. C. Goodman, J. D. Major, R. Claridge, D. P. Halliday and K. Durose, *Progress in Photovoltaics: Research and Applications*, 2014, **22**, 24–34.

155 S. Schorr, *Solar Energy Materials and Solar Cells*, 2011, **95**, 1482 – 1488.

156 L. Choubrac, M. Paris, A. Lafond, C. Guillot-Deudon, X. Rocquefelte and S. Jobic, *Phys. Chem. Chem. Phys.*, 2013, **15**, 10722–10725.

157 E. Isotta, B. Mukherjee, C. Fanciulli, N. M. Pugno and P. Scardi, *The Journal of Physical Chemistry C*, 2020, **124**, 7091–7096.

158 M. Wuttig and N. Yamada, *Nature materials*, 2007, **6**, 824.

159 W. M. andx Yamada M., *Nature Materials*, 2007, **6**, 824–832.

160 R. S., *Annual Review of Materials Research*, 2009, **39**, 25–48.

161 J. B. Williams, S. P. Mather, A. Page, C. Uher and D. T. Morelli, *Journal of Applied Physics*, 2017, **122**, 045105.

162 W. J. B. and D. T. Morelli, *J. Mater. Chem. C*, 2016, **4**, 10011–10017.

163 E. E. Shelimova, O. G. Karpinskii, P. P. Konstantinov,

M. A. Kretova, E. S. Avilov and V. S. Zemskov, *Inorganic Materials*, 2001, **37**, 342 – 348.

164 T. Rosenthal, M. N. Schneider, C. Stiewe, M. Doblinger and O. Oeckler, *Chemistry of Materials*, 2011, **23**, 4349–4356.

165 H. Wiedemeier and P. Siemers, *Zeitschrift für anorganische und allgemeine Chemie*, 1977, **431**, 299–304.

166 O. Karpinsky, L. Shelimova, M. Kretova and J.-P. Fleurial, *Journal of alloys and compounds*, 1998, **268**, 112–117.

167 J. L. Da Silva, A. Walsh and H. Lee, *Physical Review B*, 2008, **78**, 224111.